

## Article

# CoO, Cu, and Ag Nanoparticles on Silicon Nanowires with Photocatalytic Activity for the Degradation of Dyes

Olda Alexia Cárdenas Cortez <sup>1,2</sup> , José de Jesús Pérez Bueno <sup>1,\*</sup> , Yolanda Casados Mexicano <sup>1</sup>,  
Maria Luisa Mendoza López <sup>3</sup>, Carlos Hernández Rodríguez <sup>1</sup>, Alejandra Xochitl Maldonado Pérez <sup>1</sup>,  
David Cruz Alejandre <sup>2</sup>, Coraquetzali Magdalena López <sup>1,4</sup>, María Reina García Robles <sup>1</sup>, Goldie Oza <sup>1</sup> ,  
José Germán Flores López <sup>1</sup> and Hugo Ruiz Silva <sup>1</sup>

- <sup>1</sup> Centro de Investigación y Desarrollo Tecnológico en Electroquímica, S. C., Parque Tecnológico Querétaro-Sanfandila, Pedro Escobedo, Querétaro C.P. 76703, Mexico
- <sup>2</sup> Tecnológico Nacional de México, Instituto Tecnológico Superior de Poza Rica. III Ver, Luis Donaldo Colosio s/n, Ejido Arroyo del Maíz, Poza Rica de Hidalgo, Veracruz C.P. 93230, Mexico
- <sup>3</sup> Tecnológico Nacional de México, Instituto Tecnológico de Querétaro, Av. Tecnológico s/n Esq. M. Escobedo Col. Centro, Querétaro C.P. 76000, Mexico
- <sup>4</sup> Centro de Investigación y de Estudios Avanzados del Instituto Politécnico Nacional, Unidad Saltillo, Av. Industria Metalúrgica No. 1062, Parque Industrial, Ramos Arizpe, Coahuila C.P. 25900, Mexico
- \* Correspondence: jperez@cideteq.mx



**Citation:** Cárdenas Cortez, O.A.; de Jesús Pérez Bueno, J.; Casados Mexicano, Y.; Mendoza López, M.L.; Rodríguez, C.H.; Maldonado Pérez, A.X.; Cruz Alejandre, D.; Magdalena López, C.; García Robles, M.R.; Oza, G.; et al. CoO, Cu, and Ag Nanoparticles on Silicon Nanowires with Photocatalytic Activity for the Degradation of Dyes. *Sustainability* **2022**, *14*, 13361. <https://doi.org/10.3390/su142013361>

Academic Editors: Ihsanullah Ihsanullah, Mu Naushad and Muhammad Bilal

Received: 25 June 2022

Accepted: 30 September 2022

Published: 17 October 2022

**Publisher's Note:** MDPI stays neutral with regard to jurisdictional claims in published maps and institutional affiliations.



**Copyright:** © 2022 by the authors. Licensee MDPI, Basel, Switzerland. This article is an open access article distributed under the terms and conditions of the Creative Commons Attribution (CC BY) license (<https://creativecommons.org/licenses/by/4.0/>).

**Abstract:** Photocatalytic semiconductors require maintaining stability and pursuing higher efficiencies. The studied systems were silicon nanowires (Si<sub>NWs</sub>), silicon nanowires with cobalt oxide nanoparticles (Si<sub>NWs</sub>-CoO<sub>NPs</sub>), and silicon nanowires with copper nanoparticles (Si<sub>NWs</sub>-Cu<sub>NPs</sub>). Si<sub>NWs</sub> were synthesized by metal-assisted chemical etching (MACE) from silicon wafers keeping the remaining silver nanoparticles for all three sample types. The nanowires were about 23–30 μm in length. CoO<sub>NPs</sub> and Cu<sub>NPs</sub> were deposited on Si<sub>NWs</sub> by the autocatalytic reduction processes (electroless). There were many factors in the process that affect the resulting structures and degradation efficiencies. This work shows the degradation of methyl orange (MO) together with the chemisorption of methylene blue (MB), and rhodamine 6G (Rh6G) by direct illumination with visible radiation. The MO degradation kinetics were in the sequence Si<sub>NWs</sub>-Cu<sub>NPs</sub> (88.9%) > Si<sub>NWs</sub> (85.3%) > Si<sub>NWs</sub>-CoO<sub>NPs</sub> (49.3%), with the Si<sub>NWs</sub>-Cu<sub>NPs</sub> having slightly faster kinetics. However, Si<sub>NWs</sub>-CoO<sub>NPs</sub> have slow degradation kinetics. The chemisorptions of MB and Rh6G were Si<sub>NWs</sub>-Cu<sub>NPs</sub> (87.2%; 86.88%) > Si<sub>NWs</sub> (86%; 87%) > Si<sub>NWs</sub>-CoO<sub>NPs</sub> (17.3%; 12%), showing dye desorptions together with lower chemisorption capacities. This work shows iridescence in optical microscopy images by the visible light interference caused by the spaces between the nanowire bundles.

**Keywords:** nanowires; photocatalysis; silicon; water remediation; heterojunction; MACE

## 1. Introduction

In recent years, soil, air, and water bodies have been the primary concern due to the alarming increment of their contamination. Pollution comes mainly from pesticides, heavy metals, and dyes, causing severe damage to human health and altering the ecological equilibrium. Thus, quantifying these pollutants and their removal is important for protecting human wellness and environmental conservation [1]. Nowadays, the trend is to develop new technologies and materials capable of facing environmental contamination and being at the same time eco-friendly and sustainable.

The textile industry is important for many nations because materials, assembled parts, or final products are generally exported to the United States of America and the European Union. However, the textile industry contributes the most to environmental deterioration due to a large amount of water used, later converted into wastewater with a high content of harmful chemicals to humans and the ecosystems. In this industry, dyes

are challenging compounds to remove from sewage because they are present in ppm concentrations and are hardly biodegradable. Azo dyes are some of the priority dyes to remove from wastewater due to their release of chemicals. They have already been banned in the European Union. Therefore, the treatment of colored effluents becomes an issue of environmental concern. The techniques used to treat dyes in wastewater are the Fenton processes [2,3], ozonation [4], adsorption [4–8], membrane technology [4,9,10], electrochemical techniques [10], photocatalysis [11–13], and others [14–16].

Heterogeneous photocatalysis with nanostructured semiconductors has become an up-and-coming innovative technique due to its unique structures and properties [11]. This is the case with silicon nanowires [12,17–21], a nanostructure proving to be an effective photocatalyst for the oxidation of organic dyes and aromatic molecules, which exhibit higher efficiency if they are decorated with metallic nanoparticles. Here, efficiency is assumed as the conversion rate of radiative energy into breakage of atomic bonds of the pollutant molecules by transforming photons into electron–hole pairs and then into reactive oxygen species. Previous works have demonstrated the efficacy of silicon nanowires decorated with copper nanoparticles in degrading organic dyes, such as methyl orange, and reducing other chemicals, such as chromium, using visible light [12]. This, even considering that silicon in bulk is not a photocatalyst because it does not have the conduction band potential to generate OH radicals or even hydrogen peroxide. Another drawback of this nanostructured silicon with Schottky barriers is its efficiency reduction in consecutive photocatalysis cycles attributed to the increased copper oxide layer around the nanoparticles. Nonetheless, silicon is the most used semiconductor in the electronic industry and is broadly used in photovoltaics. Improving its efficiencies could make photocatalysis a feasible method of water and air treatments.

The cobalt oxides CoO and Co<sub>3</sub>O<sub>4</sub> [22,23], among other oxides such as TiO<sub>2</sub>, ZnO, or CuO, have been profusely investigated for their catalytic activities in the oxidative degradation of organic pollutants [11,13,24–28]. In addition, their catalytic activities have been analyzed for water splitting [24,25,29–31], showing an oxygen evolution reaction and CO<sub>2</sub> reduction, conducting to obtaining species, such as CH<sub>4</sub> [32,33].

Aligned with the above topics, methyl orange (MO) [1,34,35], methylene blue (MB) [15, 36–39], and rhodamine 6G (Rh6G) [16,34,40–43] are dyes frequently used to evaluate the photocatalytic activity of some semiconductors and other compounds, such as TiO<sub>2</sub>, ZnO, or reduced graphene oxide [11,13,26].

This work consists of depositing cobalt to obtain cobalt oxide nanoparticles on the silicon nanowires to cause a reduction of organic dyes using photocatalysis with visible irradiation. The proposal for cobalt oxide nanoparticles instead of copper is that cobalt oxide has been reported as photocatalytic and is already stable when exposed to oxygen from the environment, making it an excellent candidate to be stable in consecutive photocatalysis cycles. The organic dyes studied were methyl orange, methylene blue, and rhodamine 6G in a concentration of 20 ppm. The silicon nanowires were synthesized by metal-assisted etching (MACE), while the cobalt oxide nanoparticles were deposited by the electroless technique on the nanowires.

## 2. Materials and Methods

### 2.1. Preparation of the Silicon Wafers

The monocrystalline p-type silicon c-Si wafers (12.5 cm in diameter and (100) preferential crystalline direction) were cut into 2.5 × 3 cm plates with a diamond point cutter. The estimated electrical resistivity for the silicon wafers was about 0.01–0.02 Ω cm. Then, with sandpaper of SiC (average grain size of 77 μm), the silicon plates were polished on one or both sides. A deionized water drop was put before sanding and the polishing was in only one direction. The silicon plates were highly brittle, so care was put into avoiding breaking them or scratching the mirror finishing part in the polishing procedure. Finally, c-Si plates were rinsed with plenty of deionized water to remove most of the free sanding residues (incrusted residual particles).

## 2.2. Silicon Plate Cleaning

The sanded silicon plate was placed with the mirror finishing side up in a 100 mL plastic beaker. Acetone was added to the beaker until the plate was covered and sonicated for 5 min in the ultrasonic cleaning bath. The plate was rinsed with plenty of deionized water. Subsequently, ethanol was added to another glass beaker and sonicated for 5 min, followed by rinsing. Deionized water was added to another glass beaker until the plate was covered and sonicated for 10 min in the ultrasonic cleaner. Finally, the plate was left to dry at room temperature or dried with a hairdryer.

## 2.3. Synthesis of $Si_{NWs}$ by the MACE Method

The metal-assisted chemical etching (MACE) method was used to generate silicon nanowires (Figure 1) [44]. Solutions of 10% HF, Ag (5M HF/0.035 M  $AgNO_3$ ), and OX (14.1 M HF/1.9 M  $H_2O_2$ ) were prepared. The recirculating bath was set at 58 °C and the OX solution was heated for 1 h. After heating the OX solution, the cleaned silicon plates were immersed in the 10% HF solution for 20 s. Immediately after, the silicon plates were immersed in the Ag solution for 10 s. Then, they were rinsed with ultra-pure water (18 M $\Omega$ , cm, Millipore Milli-Q) to remove residues of the previous treatments. Finally, the silicon plates were immersed in the OX solution for 5 min. After that time, they were rinsed with ultra-pure water avoiding the breakage of the nanowires.

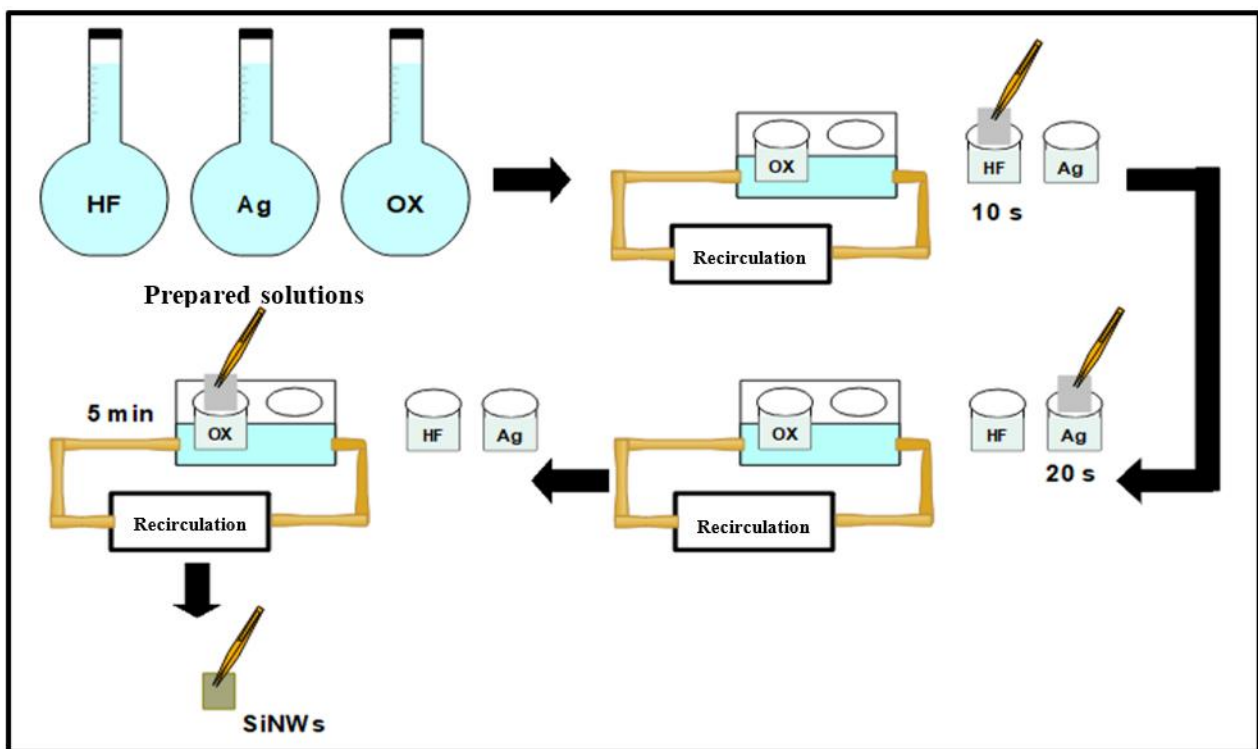


**Figure 1.** General scheme of the synthesis of  $Si_{NWs}$ .

$Si_{NWs}$  were not further treated with a nitric acid solution to remove the Ag nanoparticles located at the bottom of the nanowires. All the samples of  $Si_{NWs}$ ,  $Si_{NWs}-CoO_{NPs}$ , and  $Si_{NWs}-Cu_{NPs}$  used in this experimentation have Ag nanoparticles at the bottom in a similar size and number.

## 2.4. $CoO_{NPs}$ Deposit on $Si_{NWs}$ ( $Si_{NWs}-CoO_{NPs}$ )

Figure 2a represents the stage of the  $Si_{NWs}-CoO_{NPs}$  sample preparation. The preparation of the electroless bath consisted in mixing  $CoCl_2$  (0.1M)/ $HCHO$  (0.2M)/ $NaOH$  (9M) [45]. The plate with  $Si_{NWs}$  was immersed in the electroless bath for 5 s and rinsed

with plenty of ultrapure water to remove possible residues on the plate. Subsequently, it was left to dry at room temperature or dried with a hairdryer and stored in a Petri dish without water.

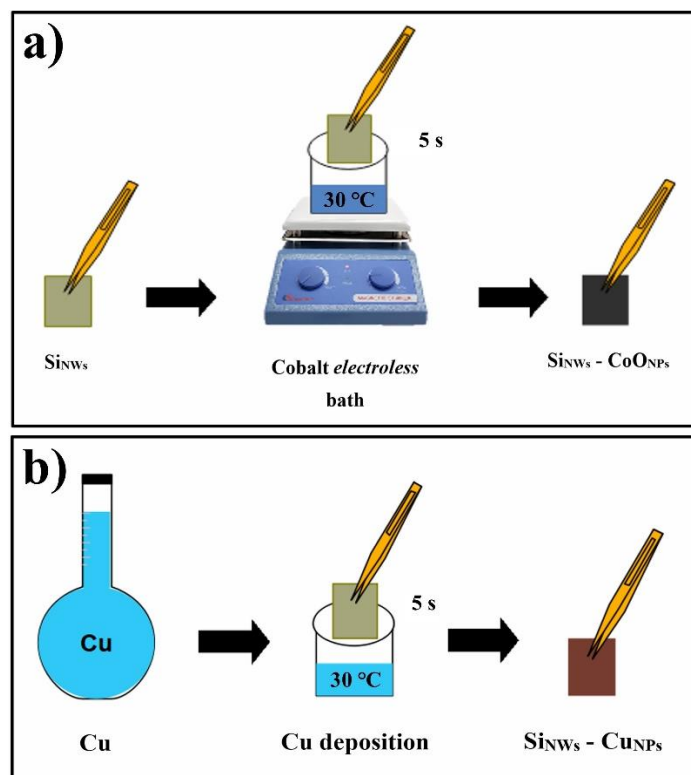


**Figure 2.** Schemes of the depositing processes for (a) CoONPs and (b) Cu on SiNWs.

### 2.5. Synthesis of SiNWs with Copper Electroless (SiNWs-CuNPs)

The absorption spectra of the solutions were obtained by a Shimadzu UV-2600 spectrophotometer with a step size of 0.5 nm.

The electroless copper deposits were made with a 0.1 M HF/CuSO<sub>4</sub> solution (Figure 2b). The plate with SiNWs was immersed for 5 s in the Cu solution. Then, it was rinsed with plenty of ultra-pure water. Finally, the SiNWs-CuNPs plate was stored in a Petri dish with deionized water to reduce copper oxidation.

### 2.6. Photocatalysis with MO, MB, Rh6G

Figure 3 represents the stages of photocatalysis experiments. Dye solutions of MO, MB, and Rh6G were prepared at 20 ppm. Then, 26 mL of the dye solution were measured and deposited in a glass crystallizer. The pH of the solutions was measured. The SiNWs-CuNPs contributed to pH reduction, with the pH of the MO solution passing from 6.2 to 4.3 on average. The glass crystallizer was placed inside the photocatalysis box, and the previously synthesized plate (SiNWs, SiNWs-CoONPs, or SiNWs-CuNPs) was inserted.

An initial sample (1.5 mL) of the dye solution was taken. Then, the photocatalysis box was covered and the lamp was turned on. Aliquots of 1.5 mL were taken from the dye solutions at 5, 15, 30, 90, 120, and 150 min. The photocatalytic box had visible LED lights installed within, with a total power of 18 W/m<sup>2</sup>. Each time the sample was taken, the LEDs were turned off and the photocatalysis box was open. The box was covered again after the samples were taken out, and the LEDs were turned on again. After 150 min, the plate was removed from the solution and rinsed with plenty of deionized water. Finally, the plate was stored in dry Petri dishes.

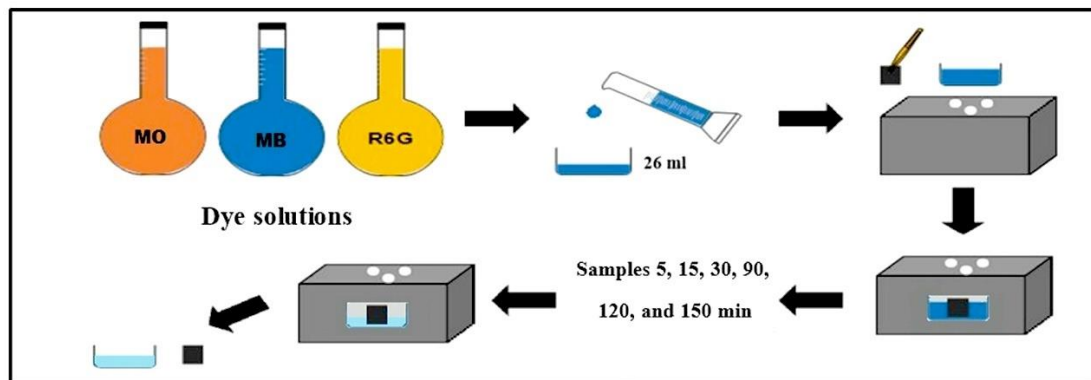


**Figure 3.** General scheme of the heterogeneous photocatalysis process.

### 2.7. Specifications of the Characterization Techniques and Experimental Setup

After being obtained, the plates with  $\text{Si}_{\text{NWs}}$ ,  $\text{Si}_{\text{NWs}}\text{-CoNPs}$ , or  $\text{Si}_{\text{NWs}}\text{-Cu}$ , were segmented with a diamond tip cutter. The plates were placed transversely with a metal holder to obtain images of the nanowires with the KEYENCE VHX-5000x digital microscope, using the compound lens objective VH-Z500R/Z500T, which has a zoom range of  $500\times\text{--}5000\times$ .

A JEOL, model JSM-6510 LV, scanning electron microscope (SEM) was used, coupled to a Bruker, model Quantax 200, energy dispersive X-ray spectrometer (EDS). Plates were placed transversely with a metal holder and adhered with conductive carbon tape. Secondary electron images, backscattered electrons, punctual EDS analysis, and element mapping were obtained.

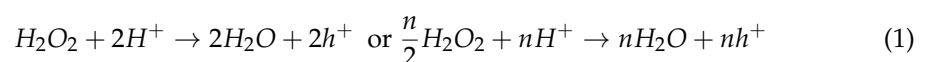
A Bruker AXS diffractometer, model D8Advance, was used with a copper X-ray source, using the  $\text{CuK}\alpha_1$  spectral line with a wavelength of  $1.5406 \text{ \AA}$  ( $8.0 \text{ keV}$ ). The measurements were performed in the detector/X-ray tube continuous coupled-mode with a step interval of  $0.04 \text{ steps}/^\circ 2\theta$ , a sweep speed of  $2.0 \text{ s/step}$ , a voltage of  $40 \text{ kV}$ , a current of  $40 \text{ mA}$ , and various intervals in the range of  $10\text{--}120^\circ 2\theta$ , were used.

The  $\text{Si}_{\text{NWs}}$ ,  $\text{Si}_{\text{NWs}}\text{-CoNPs}$ , and  $\text{Si}_{\text{NWs}}\text{-Cu}$  samples were used in photocatalysis tests with the different dye solutions. The photocatalysis cell was a black PVC box with  $12 \text{ V}$  ( $20 \text{ W/m}^2$  luminous intensity) white LEDs connected in series ( $\lambda > 450 \text{ nm}$ ,  $960 \pm 10 \text{ lx}$ ) [12]. The illuminated area of the samples was about  $5.5 \text{ cm}^2$  at a distance of about  $8 \text{ cm}$ . Samples of the solutions were taken during the tests at the following times 0, 5, 15, 30, 90, 120, and 150 min. A Shimadzu, model UV-2600, UV-Vis spectrometer was used to obtain the dye degradation spectra.

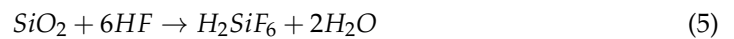
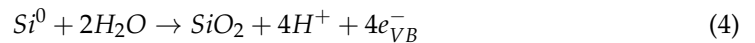
X-ray photoelectron spectroscopy (XPS) was conducted using Thermo Scientific brand equipment, model K-Alpha<sup>TM</sup>+. The pressure in the chamber was about  $10^{-9} \text{ mbar}$ , with a monochromatic X-ray source of  $\text{Al K}\alpha$  ( $1.4866 \text{ keV}$ ). The spot size of the analyses was about  $400 \text{ }\mu\text{m}$ . A step size of  $20.0 \text{ eV}$  and a total of 10 scans were used. The Advantage<sup>®</sup> software was used, fitting with the Gaussian–Lorentzian function and Shirley’s type background correlation, referenced to the C1s bond at  $284.8 \text{ eV}$  (NIST Standard Reference Database 20, version 4.1). The high-resolution spectra were taken in the ranges of C1s, O1s, Si2p, Ag3d, and Co2p.

### 2.8. Reactions of the MACE Anisotropic Wet Etching Process for $\text{Si}_{\text{NWs}}$ Formation and Nanometric Metallic Decoration

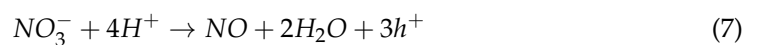
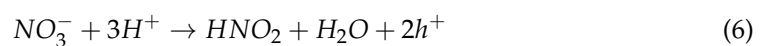
Some etching mechanisms have been proposed to explain the MACE process. A reduction reaction for the cathodic process implies the decomposition of  $\text{H}_2\text{O}_2$  at the metallic surface in acidic conditions [46–50].



The electronegativity of Ag is higher than Si, therefore, the metal ions  $Ag^+$  can withdraw electrons from silicon atoms, or equivalently the holes are generated into the silicon, taking place the deposition of metallic silver as nanoparticles on the silicon surface [49,51]:

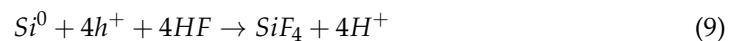


The deposited silver into the silicon surface can promote the formation of pores. It has been proposed that pore formation is caused mainly by the decomposition of nitrate ions from  $AgNO_3$ , which acts as an oxidant and metal source. Besides this, another proposed reaction includes the generation of holes due to the silver ions reduction [52]:

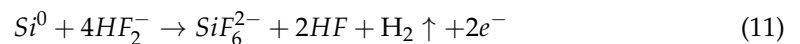


The next step is the etching of the Si layer. In this process, the silicon is oxidized to  $SiO_2$  and  $SiF_6^{2-}$ . The holes  $h^+$  generated are consumed by the silicon substrate and the anodic process occurring under the metallic deposited silver could be described as follows [46,47,50,52]:

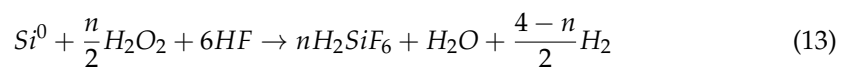
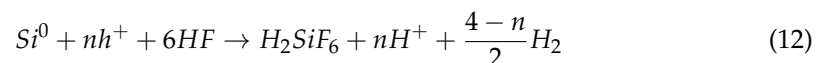
Silicon dissolution model 1:



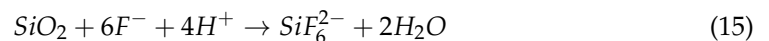
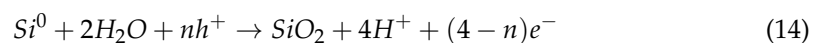
Silicon dissolution model 2:



Silicon dissolution model 3:



Silicon dissolution model 4:



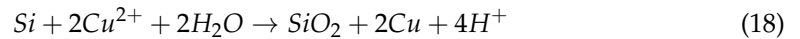
If the number  $n$  of holes equals 4, the main process will involve the production of  $SiO_2$  followed by its etching and the absence of  $H_2$ . In addition, if  $n = 2$ , there is a ratio of 1:1 between the etched silicon and one molecule of  $H_2$  formed. While the former mechanism is associated with the silicon/metal interface producing a straight etched profile, the latter can occur outside the interface and allows obtaining nanoporous silicon [47].

On the other hand, the proposed reactions for the electroless copper deposit on silicon nanowires are as follows [53]:

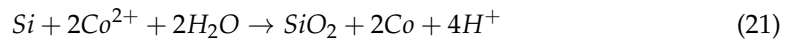
Copper reduction model 1:



Copper reduction model 2:



Furthermore, the proposed reactions for the electroless cobalt deposit and its oxidation CoO on silicon nanowires are as follows [22,23]:



### 3. Results and Discussion

#### 3.1. Characterization of the $Si_{NWs}$ - $Cu_{NPs}$ and $Si_{NWs}$ - $CoO_{NPs}$

The topography and distribution of the synthesized nanowires were observed (Figure 4). In these visualizations, the central part of the silicon plates had a more homogeneous distribution of nanowires on the silicon plate. So, the micrographs of the differently prepared samples were taken in these areas. The explanation for observing the structure using optical or electronic microscopies is that those images show bundles or conglomerates of nanowires and only such groups are visible. The diameter of each nanowire only has slight fluctuations depending on the synthesis procedure (about 70–90 nm), different from their length which depends on many process variables (about 10–80  $\mu\text{m}$ ). Therefore, the MACE method indeed generates silicon nanowires.

Figure 4 shows the micrographs of  $Si_{NWs}$ ,  $Si_{NWs}$ - $Cu_{NPs}$ , and  $Si_{NWs}$ - $CoO_{NPs}$ . Figure 4a,b show the micrographs of a silicon nanowire plate ( $Si_{NWs}$ ). In Figure 4a, the  $Si_{NWs}$  plate is seen in its cross-section, having an approximate length of 42.7  $\mu\text{m}$ . Nanowires formed vertically on the silicon plate, which were abundant and not so far apart. Figure 4b shows the top view of the  $Si_{NWs}$  plate. This micrograph shows the homogeneous distribution of the nanowires and the agglomerations that occur between them, forming small bundles. Figure 4c,d show the micrographs of a silicon nanowire plate decorated with copper nanoparticles ( $Si_{NWs}$ - $Cu_{NPs}$ ). Figure 4c shows the cross-sectional view of the nanowires with a vertical orientation on the surface of the silicon plate and a length of about 44.1  $\mu\text{m}$ .

Figure 4d shows the surface view of the  $Si_{NWs}$ - $Cu_{NPs}$  plate. There is a homogeneous distribution of nanowires and the islands formed by their agglomeration. Moreover, there is a color change on the surface due to the deposition of the copper nanoparticles. Figure 4e,f show the micrographs of a  $Si_{NWs}$  plate decorated with cobalt nanoparticles ( $Si_{NWs}$ - $CoO_{NPs}$ ). Figure 4e shows the cross-sectional view of this  $Si_{NWs}$ - $CoO_{NPs}$  plate. It should be noted that the formation of these nanowires occurred differently from the  $Si_{NWs}$  shown in Figure 4a. In this case, the nanowires were formed vertically on the silicon surface but in a highly spaced distribution, having a length of about 23.48  $\mu\text{m}$ . Figure 4f shows the superficial view, which shows the spacing between the nanowires (the bright points or areas correspond to nanowires). The micrograph has different color compared with that of the  $Si_{NWs}$  and this is caused by the cobalt nanoparticles deposited on the nanowire surfaces.

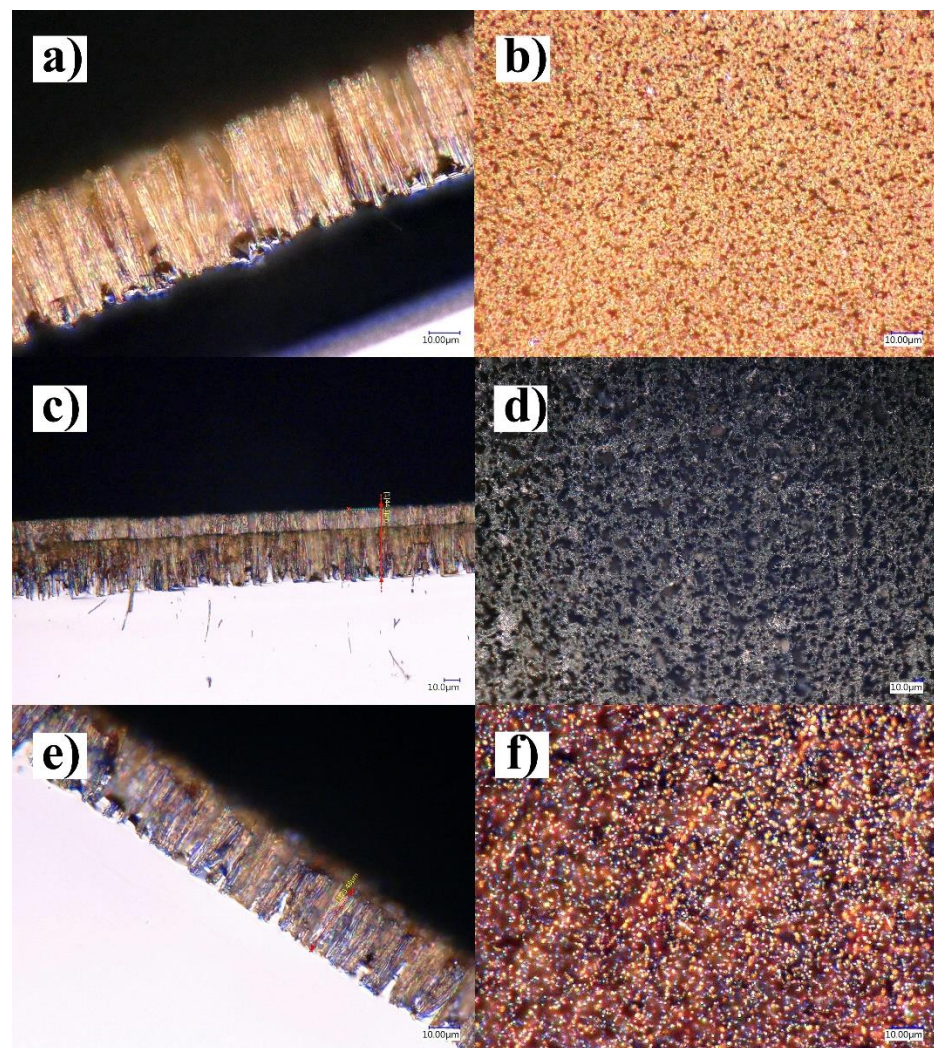


**Figure 4.** Micrographs were taken using a digital optic microscope with a 10.00  $\mu\text{m}$  scale bar.  $\text{Si}_{\text{NWs}}$  sample (a) transverse view at 2000 $\times$  and (b) 2000 $\times$  superficial view.  $\text{Si}_{\text{NWs}}-\text{Cu}_{\text{NPs}}$  sample (c) transverse view at 1000 $\times$ , and (d) surface view at 500 $\times$ .  $\text{Si}_{\text{NWs}}-\text{Co}_{\text{NPs}}$  sample (e) transverse view at 2000 $\times$  and (f) surface view at 2000 $\times$ .

In the optical images, there is the phenomenon of interference, observed as iridescent colors, because of the size of the filaments resulting from the MACE method and the space between them, which, as far as we know, this work is the first or between the few that show interference of visible light in the nanostructured bundles (Figure 4a,c,e,f), when observing them by Digital Optic Microscopy using 1000 $\times$ –5000 $\times$ . The rainbow-colored images resulted from the visible light of the microscope, causing interference when passing across the groups and between the nanowires according to the interference Equations (1) and (2) [54], maximum and minimum, respectively.

$$d = \frac{(2m + 1)\lambda}{4n} \quad (24)$$

$$d = \frac{m\lambda}{2n} \quad (25)$$

where,  $d$  is the optical thickness,  $n$  is the refractive index,  $\lambda$  is the wavelength, and  $m$  is an integer number (order of interference).

The silver, copper, and cobalt metallic particles were grown by the electroless method, which implies no use of an imposed external potential. Even more, no activation agents

were used to seed the silicon surface and grow the metallic crystals. Therefore, the metallic ions were reduced both by the HF-treated silicon [17] and by electrons on the silicon surface, which were promoted from the valence band when absorbing light since the silicon had p-type doping and had no electrons in excess. The electroless method has a limited capability of increasing the mass of deposited metals beyond the nanometric scale (1–100 nm) because once the nucleation sites were covered, the potentials on these areas change and the active sites for further reductions diminish. Usually, the galvanic replacement reaction is followed by one or two electrolytic depositions to thicken the coatings. Consequently, the size of electroless grown metallic particles in about 10 s for silver, 5 s for cobalt, and 5 s for copper were nanometric in size [12,17,55].

Using scanning electron microscopy (SEM), the formation and structure of the synthesized silicon nanowires were observed in more detail. Moreover, the samples were analyzed using energy dispersive X-ray spectroscopy (EDS) to obtain the elemental mapping.

Figure 5 shows the SEM micrographs with a 10.00  $\mu\text{m}$  scale bar and elemental point analysis on the cross-sectional area by EDS. Moreover, the figure shows the elemental mapping over the cross-sectional of the  $\text{Si}_{\text{NWs}}\text{-Co}_{\text{NPs}}$  sample. Figure 5a shows the SEM micrograph of the  $\text{Si}_{\text{NWs}}$  sample at 1500 $\times$ . In this secondary electron image, the length of the nanowires of about 32  $\mu\text{m}$  is shown. Moreover, this image shows how the nanowires were agglomerated, forming small bundles. Some nanowires were broken, and some can have flexions during the process of silicon etching. The concentration of  $\text{H}_2\text{O}_2$  directly influences the morphology of the nanowires. On the other hand, Figure 5b, a micrograph made with backscattered electrons, gives a change in contrasts that allows observing the silver deposited at the base of the nanowires (bright white areas and dots). In some cases, the etching with HF, used to form nanowires, resulted in the silver nanoparticle agglomeration or dendritic forms. Part of the photocatalysis was attributed to these silver structures at the bottom of the nanowires. The silver–silicon junction, a Schottky barrier, is proposed as a higher efficient electron transferor when shaped as dendrites because the sharp shape has a lower work function, which means that it is easier to extract electrons from the pick than from a flat or round shape. In some other works, the silver or metal used to shape the structures is washed away with a nitric acid solution. Nonetheless, we agree with the works that propose that such a Schottky barrier contributes to photocatalysis.

EDS analysis was performed on the cross-sectional area of the  $\text{Si}_{\text{NWs}}$  sample on the yellow rectangle of Figure 5a. The elements present were Si, C, O, and Ag in percentages of 80.14%, 12.71%, 3.96%, and 3.19%, respectively. C and O presence in the sample was attributed to the contamination when in contact with the atmosphere. Moreover, the oxygen present was related to the formation of oxides, in this case, with the Si. The samples of  $\text{Si}_{\text{NWs}}\text{-Cu}_{\text{NPs}}$  were also characterized by SEM at 2000 $\times$  and the micrographs are shown in Figure 5d,e. Figure 5d is an image of secondary electrons showing the nanowires with a length of about 48  $\mu\text{m}$ . The nanowires were assembled into small bundles. Figure 5e was made with backscattered electrons showing contrasts between the silver deposited at the base of the nanowires in the form of dendrites (bright white areas) and the copper nanoparticles that decorate the tips of the nanowires (bright points). Figure 5f shows the elemental EDS analysis of  $\text{Si}_{\text{NWs}}\text{-Cu}_{\text{NPs}}$  on the yellow rectangle area in Figure 5h. In this case, the elements present in the sample were Si, O, Cu, and Ag in a percentage of 83.27%, 11.41%, 3.28%, and 2.03%, respectively. The presence of copper in the sample indicates the deposition of copper nanoparticles on the nanowires. In this case, in addition to a  $\text{SiO}_2$  layer on top of the silicon, the oxygen can be attributed to a layer of copper oxides on top of the nanoparticles.

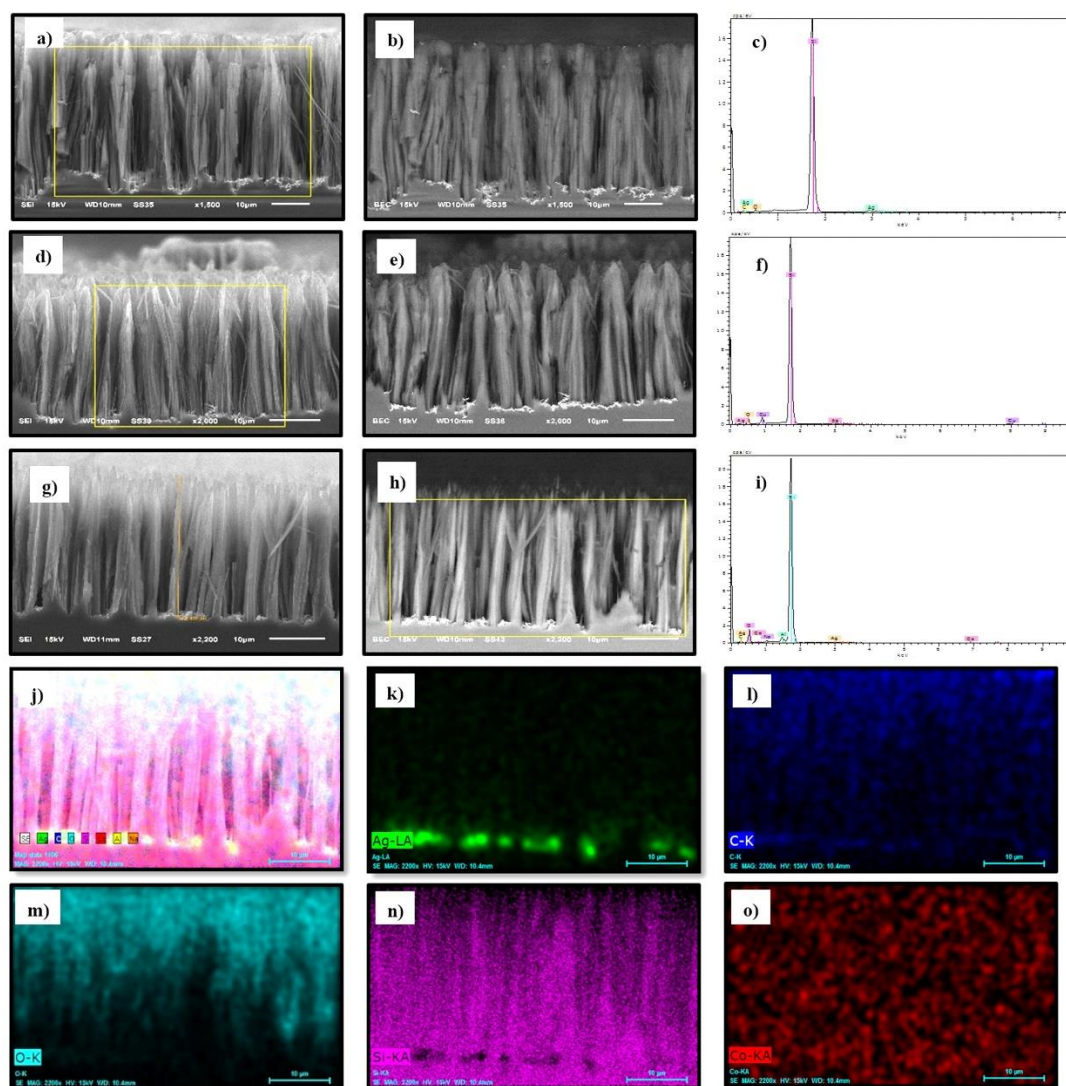


**Figure 5.**  $\text{Si}_{\text{NWs}}$  sample: (a) Cross-section micrograph of secondary electrons at  $1500\times$ , (b) Cross-section micrograph of backscattered electrons at  $1500\times$ , and (c) EDS of the  $\text{Si}_{\text{NWs}}$  sample.  $\text{Si}_{\text{NWs}}\text{-Cu}_{\text{NPs}}$  sample: (d) Cross-section micrograph of secondary electrons at  $2000\times$ , (e) Cross-section micrograph of backscattered electrons at  $2000\times$ , and (f) EDS of the  $\text{Si}_{\text{NWs}}\text{-Cu}_{\text{NPs}}$  sample.  $\text{Si}_{\text{NWs}}\text{-Co}_{\text{NPs}}$  sample: (g) Cross-section micrograph of secondary electrons at  $2200\times$ , (h) Cross-section micrograph of backscattered electrons at  $2200\times$ , and (i) EDS of the  $\text{Si}_{\text{NWs}}\text{-Co}_{\text{NPs}}$  sample synthesized in an electroless bath with  $0.01\text{ M CoCl}_2$ .  $\text{Si}_{\text{NWs}}\text{-Co}_{\text{NPs}}$  sample: (j) elemental mapping over the cross-sectional area by EDS. The analyzed areas are indicated with yellow rectangles. The EDS mapping of the  $\text{Si}_{\text{NWs}}\text{-Co}_{\text{NPs}}$  sample corresponds to (k) Ag, (l) C, (m) O, (n) Si, and (o) Co.

The  $2200\times$  SEM micrographs of the synthesized  $\text{Si}_{\text{NWs}}\text{-Co}_{\text{NPs}}$  are shown in Figure 5g,h. Figure 5g is an image generated by secondary electrons, where the length of the nanowires is about  $30\ \mu\text{m}$ . It is observed that the clusters of agglomerated nanowires at the bottom have a different thickness than at the top, so they end in a tip. On the other hand, Figure 5h shows the contrast of the silver in the form of dendrites (bright white areas in the SEM micrograph of backscattered electrons), that, after the formation of nanowires, remained in the bottom. These silver structures were not removed by washing with a nitric acid solution because they can contribute to photocatalysis.

In the reviewed literature, there were no reports of silver dendrites at the bottom of nanowires. In the elemental EDS analysis of the  $\text{Si}_{\text{NWs}}\text{-Co}_{\text{NPs}}$  (Figure 5i), corresponding to the area of the yellow rectangle of Figure 5h, the elements present in the sample were Si,

O, C, Ag, Al, Na, and Co in a percentage of 62.59%, 20.25%, 14.27%, 1.30%, 1.12%, 0.41, and 0.06%, respectively. The presence of cobalt in the sample is an indicator of the deposition of cobalt on the nanowires, although its percentage is low due to the concentration of 0.01 M of  $\text{CoCl}_2$  in the electroless bath. However, the EDS analysis did not confirm the oxidation state of cobalt, identifying it as metallic or oxidized. The presences of Al and Na were because of residues generated in the  $\text{Si}_{\text{NWs}}$  formation process. Na was part of the composition of the electroless bath and  $\text{Al}_2\text{O}_3$  was an inlaid residue of the plate sanding. The distributions by zones of each element are shown in Figure 5j, where the elemental mapping of the  $\text{Si}_{\text{NWs}}\text{-CoONPs}$  is shown.

The growth process of silver dendritic structures in the nanowire formation process was observed with SEM. Figure 6 shows the Ag dendritic structures observed on p-type monocrystalline silicon (c-Si) substrate immersed for 10 s into a mixture of HF (5M)/ $\text{AgNO}_3$  (0.035M) in an aqueous solution. Figure 6a shows a cross-sectional view of the surface composed of  $\text{Ag}_{\text{NPs}}$  and  $\text{Si}_{\text{NWs}}$ . Figure 6b shows that the silicon substrate was covered with nanoparticles and dendrites of Ag. Moreover, this image gives evidence of a diversity of shapes of the crystalline dendrites and branches. The uniformity of a large number of such structures is illustrated in Figure 6c, showing that the products consist almost entirely of spike-shaped Ag dendrite crystals. Figure 6d shows the random orientation of the Ag crystals obtained by transforming the nanoparticles used initially for shaping the nanowires.

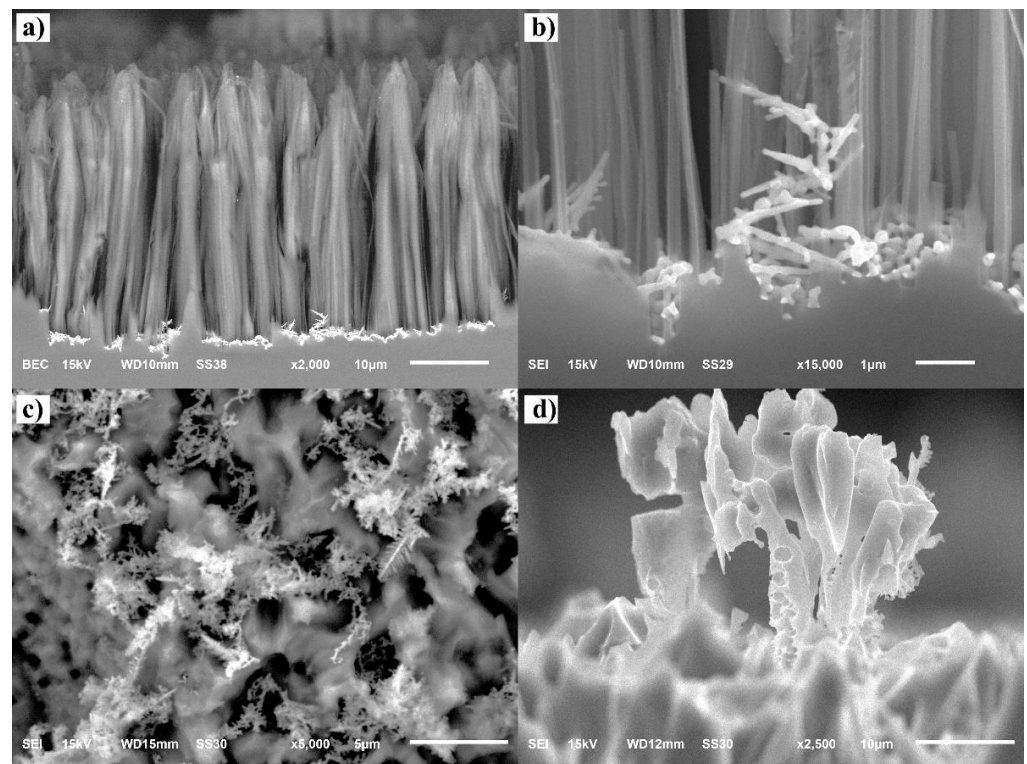


**Figure 6.** SEM images of c-Si (p-type) substrate after dipping into the HF (5M)/ $\text{AgNO}_3$  (0.035M) aqueous solution for 10 s. (a) Cross-section micrograph of backscattered electrons at 2000 $\times$ , (b) cross-section micrograph of secondary electrons at 15,000 $\times$  of the surface composed of nanoparticle and dendrites of Ag, (c) surface view micrograph of secondary electrons at 5000 $\times$ , and (d) Cross-sectional micrograph of secondary electrons at 15,000 $\times$  of a structure formed from Ag particles.

The Ag dendrite formation process is caused by the galvanic displacement reaction consisting of redox reactions that occur simultaneously on the silicon surface. The cathodic reaction reduces  $\text{Ag}^+$  on the Si wafer surface by injecting holes into the valence band of Si and generating Ag metallic particles. The anodic reaction results in the oxidation

and dissolution of Si adjacent to Ag particles [56]. During the displacement reaction, the amorphous phase leads to rapid and continuous deposition on the surface of the growing particles, and several randomly oriented Ag particles spontaneously crystallizing from the amorphous phase. The Ag particles randomly oriented realign and grow in preferential directions, eventually forming single crystal dendrites. The growth rate, morphologies, and structures of Ag dendrites are highly dependent on  $\text{Ag}^+$  ion concentration ( $\text{AgNO}_3$ ), reaction time, and deposition temperature.

Figure 7a shows the diffractogram of the  $\text{Si}_{\text{NWs}}$  surface. The diffractogram shows diffraction peaks at  $33.038^\circ$  and  $69.13^\circ$ , both peaks belong to the planes (2 1 1) and (4 0 0) of the Si (JCPDS 01-072-1088 and JCPDS 01-75-0589). The plane (4 0 0) of cubic silicon located at  $69.13^\circ$  of  $2\theta$  coincides with that reported by articles that use the same synthesis method [57]. Although, in this case, that peak is not the preferential direction since the  $33.038^\circ$  of  $2\theta$  peak corresponding to the Si plane (2 1 1) has a higher intensity. The change in the intensity of the peaks of silicon was attributed to the presence of the nanostructures. Moreover, there is a  $25^\circ$  peak associated with the presence of  $\text{SiO}_2$  generated by synthesizing the nanowires. The noise generated in the peak was due to the lack of a well-defined crystal structure.

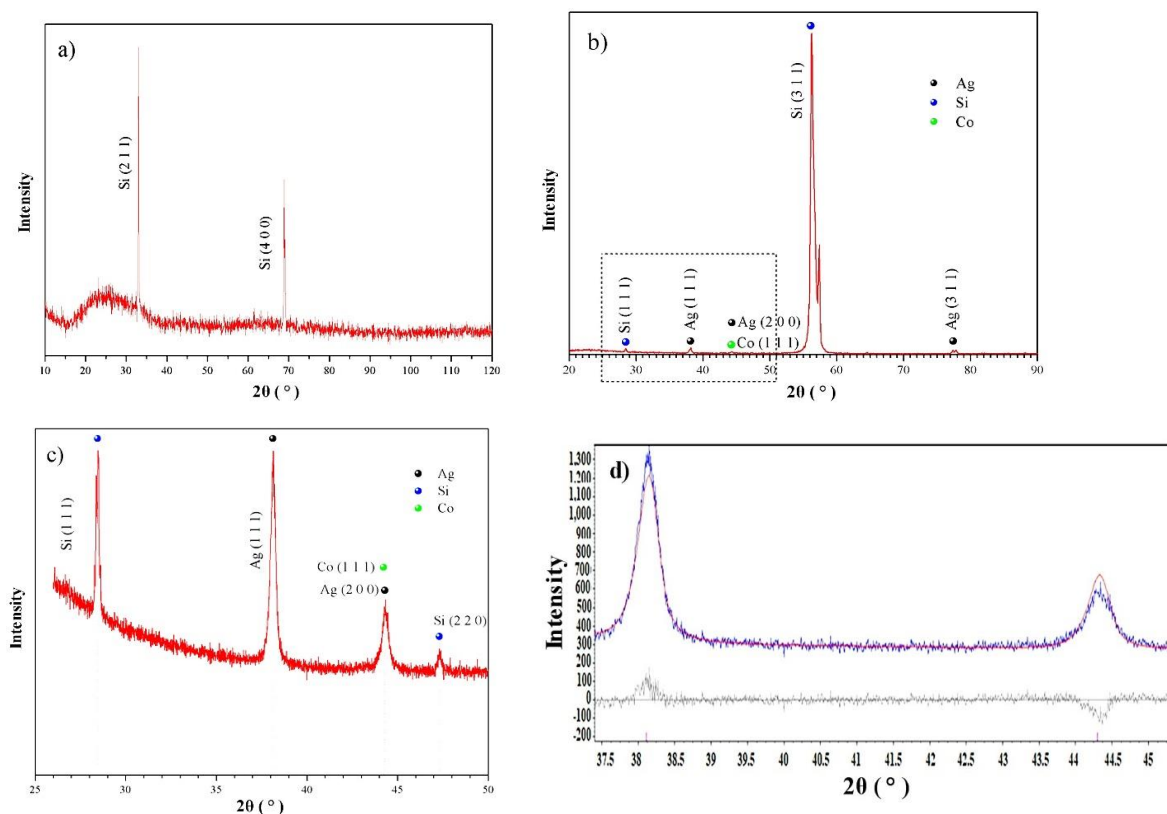


**Figure 7.** Surface diffractograms of  $\text{Si}_{\text{NWs}}\text{-CoONPs}$  (a) Coupled diffraction mode for  $10\text{--}120^\circ$   $2\theta$ . (b) Grazing-incidence diffraction mode, X-ray tube angle  $1^\circ$   $2\theta$ , range  $2\text{--}120^\circ$   $2\theta$ . (c) Grazing-incidence diffraction mode, X-ray tube angle  $4^\circ$   $2\theta$ , range  $26\text{--}50^\circ$   $2\theta$ . (d) Rietveld refinement in the range of  $37.5\text{--}45.5^\circ$   $2\theta$  showing Ag.

Figure 7b shows the diffractogram of the surface of  $\text{Si}_{\text{NWs}}\text{-CoONPs}$  performed in grazing-incidence diffraction mode with a tube position at  $1^\circ$ , in a range from  $2^\circ$  to  $120^\circ$  of  $2\theta$ , using a voltage and current of 40 kV and 40 mA, respectively. The diffractogram shows different diffraction peaks, the peaks at  $28.44^\circ$  and  $56.12^\circ$  belong to the planes (1 1 1) and (3 1 1) of the Si (JCPDS 01-75-0589). The peaks at  $38.12^\circ$ ,  $44.3^\circ$ , and  $77.399^\circ$  belong to the planes (1 1 1), (2 0 0), and (3 1 1) of the cubic Ag (JCPDS 01-065-2871), respectively. The peak at  $44.23^\circ$  is associated with the plane (1 1 1) of the Co (JCPDS 01-089-4307). Compared to the coupled mode diffractogram, the change in Si diffraction peaks can be observed on the

surface of  $\text{Si}_{\text{NWs}}\text{-CoO}_{\text{NPs}}$ . The preferential orientation of Si was in the plane (1 1 1) but the (3 1 1) shows an interference phenomenon [58,59] with the higher intensity occurring at  $56.12^\circ$  and not in the (2 1 1), as in the pattern of silicon powder. This interference can have possible additional peaks around the value of the central position. The appearance of the plane (1 1 1) was seen at  $28.44^\circ$ . There were probably slight alterations in the unit cells that the flexing of the  $\text{Si}_{\text{NWs}}$  can cause. The stress caused by these flexes would make the unit cell smaller on one side and larger on the opposite.

Figure 7c was in grazing-incidence diffraction mode with a tube position at  $4^\circ 2\theta$ , in a smaller range of  $26^\circ$  to  $50^\circ$  of  $2\theta$ . The higher resolution allows appreciating better the peaks already seen in Figure 7b. Moreover, it will enable observing the appearance of a new peak corresponding to the Si plane (2 2 0) at  $47.305^\circ$ . However, the plane (1 1 1) of the Co and the plane (2 0 0) of the Ag overlapped in the same peak. So, to determine if both elements were present, the Rietveld refinement was used (Figure 7d). By using the Rietveld refinement, the fitting was 100% with the Ag pattern and because the intensity of the peak in the adjustment (red line) was over that of the experimental diffractogram, it was not considered that Co (1 1 1) was present.

X-ray photoelectron spectroscopy (XPS) was used to determine the surface composition and oxidation states of a  $\text{Si}_{\text{NWs}}\text{-CoO}_{\text{NPs}}$  sample. Figure 8a shows the complete XPS or survey spectrum and the identified elements were Si, C, O, Ag, and Co. In the  $\text{Si}2p$  signal (Figure 8b), two peaks were found at 99.9 eV and 104 eV corresponding to Si and  $\text{SiO}_2$ , respectively. On the other hand, in the  $\text{C}1s$ , two signals were observed at 285.9 eV and 289.9 eV (Figure 8c). These signals are typical of adventitious carbon contamination, so carbon was not part of the sample. Figure 8d shows the  $\text{O}1s$  region with a single peak at 533.6 eV, corresponding to the CO bonds. It has a small shoulder at about 530.5 eV attributed to metal oxides, in this case, Co. Likewise, Figure 8e shows the  $\text{Ag}3d$  region having two signals at 368.2 eV and 374.2 eV. These two peaks are within the range 378–366 eV that can be associated with metallic silver, while the strongest signal occurs at 368.2 eV and corresponds to the characteristic signal of metallic silver. Finally, in the  $\text{Co}2p$  region (Figure 8f), there are four peaks at 782.48 eV, 787.0 eV, 798.08 eV, and 803.78 eV. It can be noted that none of these peaks correspond to metallic Co, so all the deposited Co by electroless was oxidized in the process. The obtained spectrum in this sample can coincide with  $\text{Co}(\text{OH})_2$  and  $\text{CoO}$ , but the difference between these signals is at most 1 eV, so the analysis was not conclusive, although it is very likely that both were present.

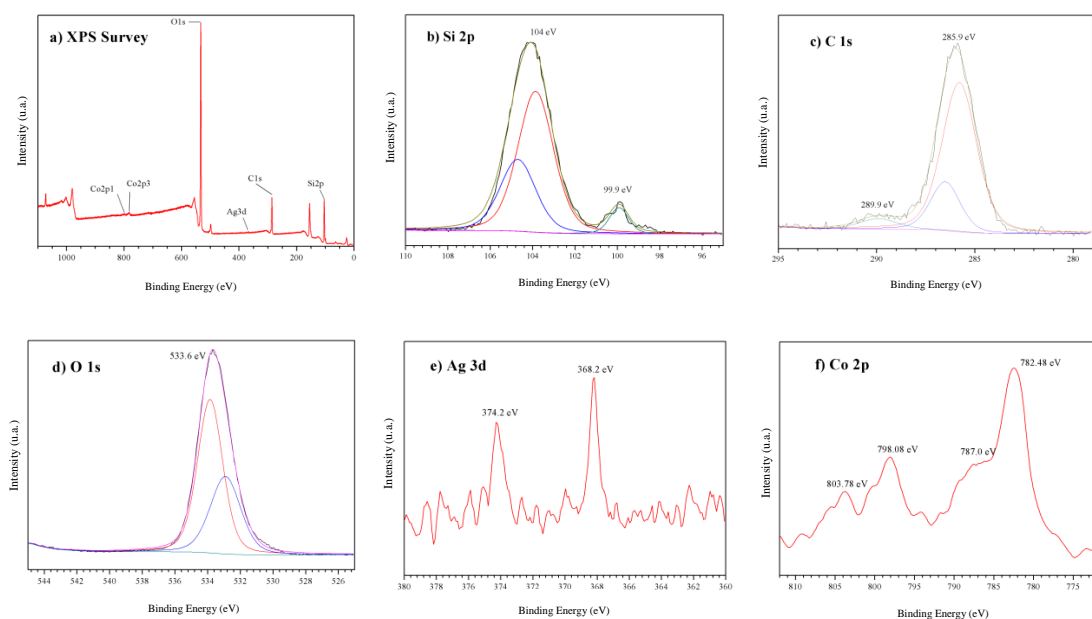


Figure 8. XPS spectra of the surface of  $\text{Si}_{\text{NWs}}\text{-CoO}_{\text{NPs}}$ .

The reason for the Co deposit not being in its metallic form was attributed to the fact that during the synthesis process, the pH of the electroless solution was 14. The Pourbaix diagram of Co in aqueous solutions [34] indicates that  $\text{Co}^{2+}$  ions in an aqueous solution are below pH 9. At pH 14, there is a high concentration of OH ions forming  $\text{Co}(\text{OH})_2$ .

### 3.2. Heterogeneous Photocatalysis

For heterogeneous photocatalysis experiments, solutions having 20 ppm of MO, MB, and Rh6G were used as organic molecules for degradation. The photocatalysts used were  $\text{Si}_{\text{NWs}}$ ,  $\text{Si}_{\text{NWs}}\text{-Cu}_{\text{NPs}}$ , and  $\text{Si}_{\text{NWs}}\text{-CoO}_{\text{NPs}}$ . After photocatalysis, the collected samples were analyzed using a UV-Vis spectrophotometer, which showed the degradation of the MO and the chemisorption of MB and Rh6G.

Firstly, the dye calibration curves were experimentally obtained to know the changes made in the degradation of MO, MB, and Rh6G (Figure 9). Solutions with different concentrations were made and they were 2, 4, 6, 8, 10, 12, 14, 16, 18, and 20 ppm for each dye. Three different aliquots were taken for each solution. Then, the absorption spectra of the solutions were taken. From the obtained curves, the highest absorption peaks of the dyes were taken as reference points, which were 464 nm, 663 nm, and 526 nm for MO, MB, and Rh6G, respectively. In addition, an average was made with the maximum absorbance values of the three aliquots taken for each concentration that were plotted with the dye concentrations. Finally, a linear adjustment was made to the experimental data to generate the calibration curves of the three dyes, estimating the reduction in the concentration of the dyes after photocatalysis with  $\text{Si}_{\text{NWs}}$ ,  $\text{Si}_{\text{NWs}}\text{-Cu}_{\text{NPs}}$ , and  $\text{Si}_{\text{NWs}}\text{-CoO}_{\text{NPs}}$ .

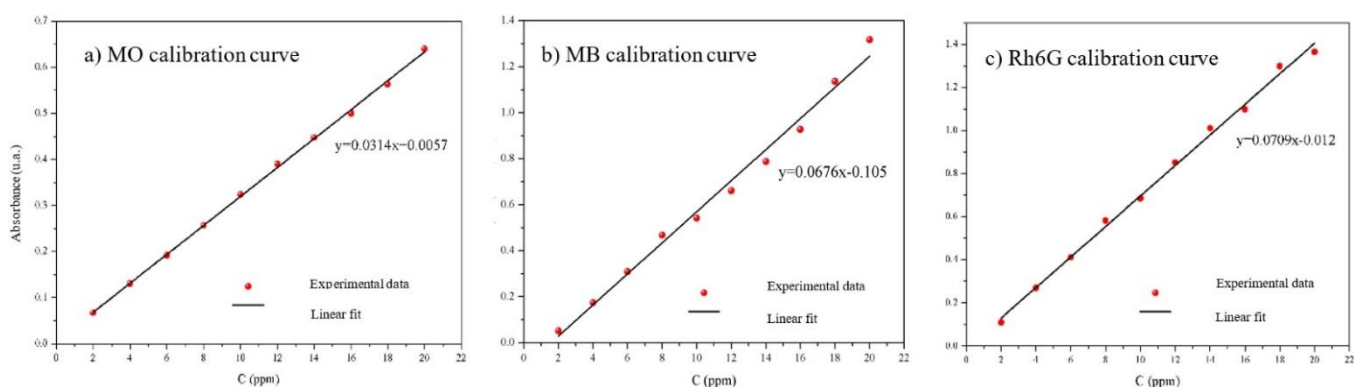


**Figure 9.** The dyes calibration curves of (a) MO, (b) MB, and (c) Rh6G.

### 3.3. Photocatalysis with MO

Recurrently have been observed that  $\text{Si}_{\text{NWs}}$  cause water splitting, which collaterally causes the pH reduction from 6.2, in the MO solution, to 4.3 on average. Figure 10 shows the photocatalytic activities of the  $\text{Si}_{\text{NWs}}$ ,  $\text{Si}_{\text{NWs}}\text{-Cu}_{\text{NPs}}$ , and  $\text{Si}_{\text{NWs}}\text{-CoO}_{\text{NPs}}$  with the MO using a white LED light. In this figure, the characteristic absorption peak of the MO at 464 nm decreases over time with the photocatalytic treatment, which is indicative of MO degradation. The maximum photocatalysis time was 150 min. This decrease in intensity occurs with the three photocatalysts ( $\text{Si}_{\text{NWs}}$ ,  $\text{Si}_{\text{NWs}}\text{-Cu}_{\text{NPs}}$ , and  $\text{Si}_{\text{NWs}}\text{-CoO}_{\text{NPs}}$ ), suggesting a similar photocatalytic degradation process. However, it was observed that in the case of the  $\text{Si}_{\text{NWs}}\text{-Cu}_{\text{NPs}}$  samples, the degradation of the MO was higher when reaching 150 min.

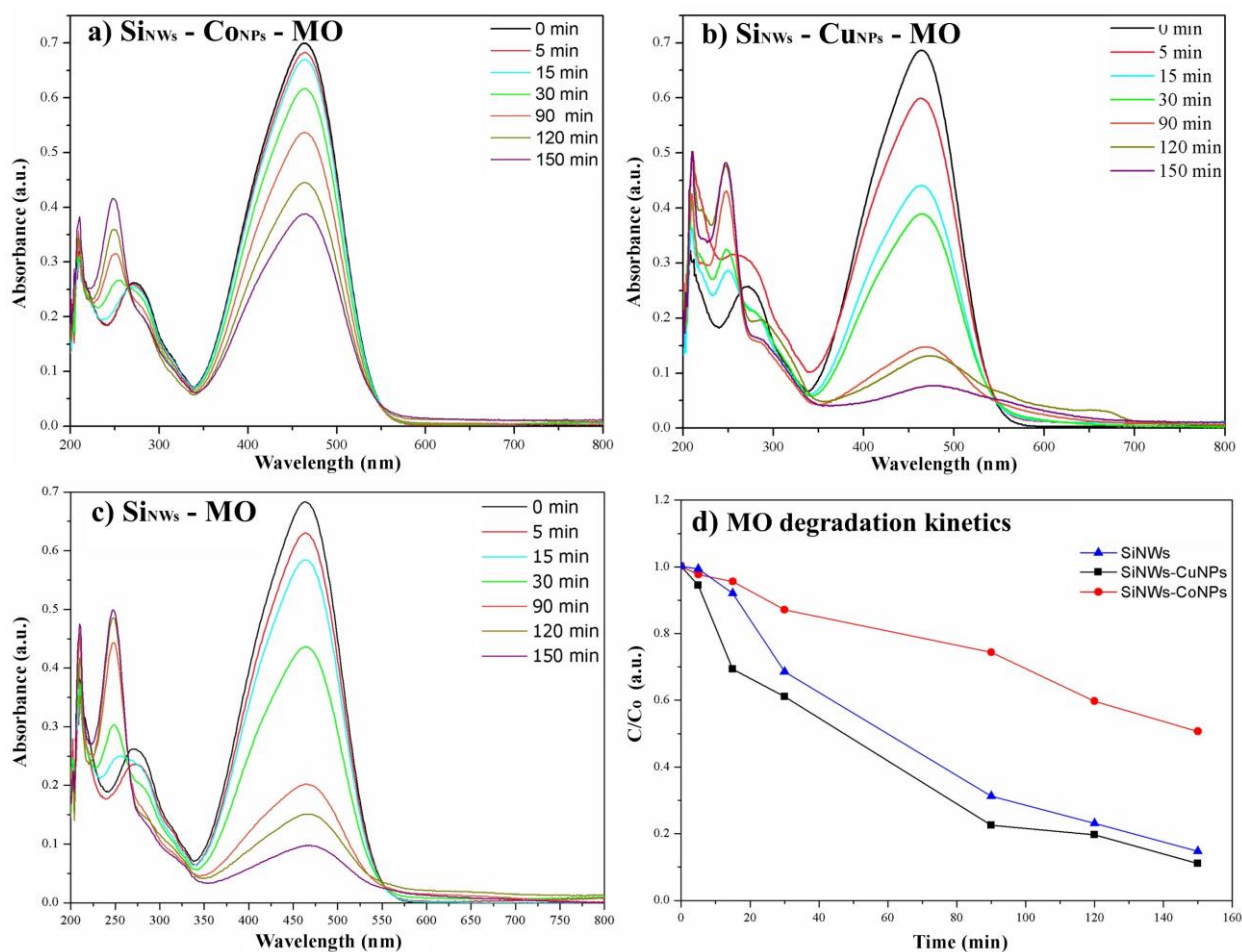


**Figure 10.** UV-Vis spectra of MO treatment with the photocatalysts (a) SiNWs, (b) SiNWs-CuNPs, and (c) SiNWs-CoNPs. (d) MO degradation kinetics using SiNWs, SiNWs-CoNPs, and SiNWs-CuNPs as photocatalysts.

Figure 10d compares the photocatalytic activity with SiNWs and SiNWs-CoNPs have efficiencies at 150 min of 85.3% and 49.3%, respectively. The degradation efficiency of SiNWs-CuNPs ranges from 5.5% at 5 min to 88.9% at 150 min, which makes it the most efficient photocatalyst.

The degradation mechanisms of MO, MB, and Rh6G have been extensively investigated [27,28], which altogether with their other characteristics make them usual targets for testing catalysts.

In the spectra of Figure 10a, while the absorbance intensity decreases at 464 nm ( $\lambda$  corresponding to the azo bond), there was an increase in intensity at 448 nm ( $\lambda$  related to the amino group). This indicates a reduction in the concentration of the azo bonds, promoting the formation of the amino groups [60].

When comparing the efficiency of the three photocatalysts, the degradation kinetics of the SiNWs-CuNPs exhibit a behavior almost parallel to the SiNWs. However, the kinetics of SiNWs-CuNPs was slightly faster, having a rate constant ( $k$ ) of about  $-0.14$  compared with  $-0.012$  of SiNWs, attributed to the contribution of Cu metallic nanoparticles deposited on their surface. Contrarily, when comparing SiNWs-CoNPs with SiNWs, there was a higher reduction in the rate of degradation kinetics. This was attributed to the CoO nanoparticles, which were not separating electron-hole pairs to contribute to the degradation of the organic molecule of the MO. Table 1 shows that all the reactions in this study were of order 1 for the three semiconductor systems with each of the three dyes.

**Table 1.** Calculations of the reaction order,  $R^2$ , and rate constant ( $k$ ) for the tests with methyl orange, methylene blue, and rhodamine 6G.

	Order	Methyl Orange		Methylene Blue		Rhodamine 6G	
		$R^2$	$k$	$R^2$	$k$	$R^2$	$k$
$\text{Si}_{\text{NWs}}\text{-Cu}_{\text{NPs}}$	1	0.983	−0.01416	0.9719	−0.014	0.983	−0.0134
	2	0.927	774.45	0.9738	820.43	0.8706	623.185
$\text{Si}_{\text{NWs}}$	1	0.997	−0.0129	0.694	−0.0129	0.829	−0.013
	2	0.94	583.75	0.4742	625.78	0.655	570.47
$\text{Si}_{\text{NWs}}\text{-Co}_{\text{NPs}}$	1	0.978	−0.00435	0.746	−0.0016	$6.88 \times 10^{-5}$	$-7.26 \times 10^{-6}$
	2	0.953	99.238	0.743	27.80	$6.99 \times 10^{-6}$	0.040

### 3.4. Photocatalysis with MB

Figure 11 shows the photocatalytic activity in the MB of the  $\text{Si}_{\text{NWs}}$ ,  $\text{Si}_{\text{NWs}}\text{-Cu}_{\text{NPs}}$ , and  $\text{Si}_{\text{NWs}}\text{-Co}_{\text{NPs}}$  with LED light. In this figure, the MB chemisorption was observed as the intensity decreases at its characteristic absorption peak, at 663 nm. However, the intensity of that peak does not decrease over time. Similar to the UV-Vis spectrum of  $\text{Si}_{\text{NWs}}$ , the intensity of the peak increases after 90 min instead of decreasing. The same happened at different times in the absorption spectrum of  $\text{Si}_{\text{NWs}}\text{-Co}_{\text{NPs}}$ .

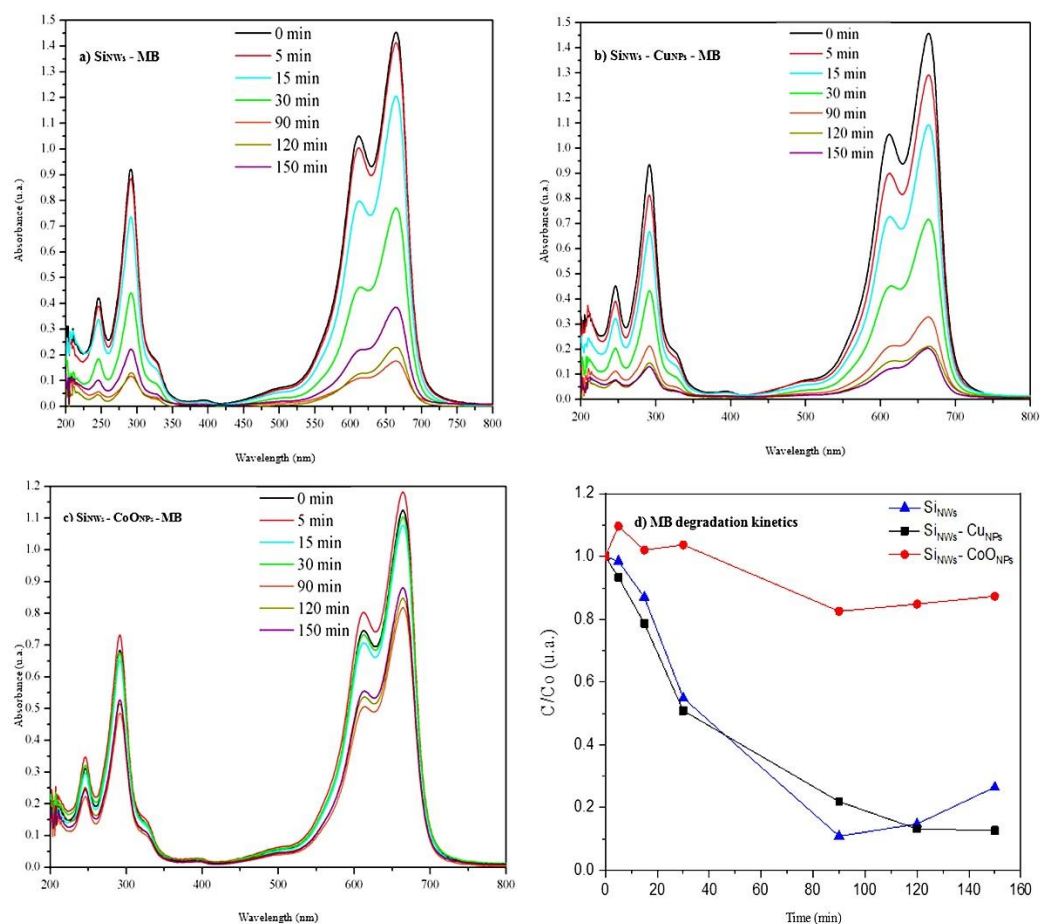


**Figure 11.** UV-Vis spectra of MB treatment with the photocatalysts (a)  $\text{Si}_{\text{NWs}}$ , (b)  $\text{Si}_{\text{NWs}}\text{-Cu}_{\text{NPs}}$ , and (c)  $\text{Si}_{\text{NWs}}\text{-Co}_{\text{NPs}}$ . (d) MB degradation kinetics using  $\text{Si}_{\text{NWs}}$ ,  $\text{Si}_{\text{NWs}}\text{-Co}_{\text{NPs}}$ , and  $\text{Si}_{\text{NWs}}\text{-Cu}_{\text{NPs}}$  as photocatalysts.

Brik et al. [61], using silicon nanowires for MB degradation, found a 21% reduction attributed to molecule absorption on the surface. They show significant changes in the

degradation percentages even using a UV source. Ameen et al. [62] attribute the dye reduction in the dark, using  $\text{Si}_{\text{NWs}}$  as a photocatalyst, to the retention of the molecules by the large surface area of the nanowires.

Figure 11d compares the photocatalytic activities of the three photocatalysts. The highest chemisorption efficiency of  $\text{Si}_{\text{NWs}}\text{-Cu}_{\text{NPs}}$  was 87.2% at 150 min. This was the only photocatalyst with different behavior. The highest chemisorption efficiency of  $\text{Si}_{\text{NWs}}$  was 86% at minute 90 because, by minute 50, their efficiency decreased to 73%. In the case of the  $\text{Si}_{\text{NWs}}\text{-Co}_{\text{NPs}}$  photocatalyst, its maximum chemisorption efficiency was 17.3% at minute 90 and by the end of the period, its efficiency decreased to 12.6%.

The UV-Vis absorption spectra of the photocatalysts show that the peak at 663 nm decreased and that there were no new peaks. So, in the case of MB, it was attributed that the phenomenon was not the degradation but the adsorption of organic molecules [60]. Moreover, the desorption of the molecules was shown, which explains why the absorbance increases at certain times of photocatalysis [16]. This process was identified as chemisorption and that behavior was attributed to a combination of absorption/desorption regulated by the changing parameters of the solution. The absence of degradation of the organic molecules was attributed to the lack of the potential necessary to break the bonds of that molecule with three aromatic rings. As with MO, the highest decoloration was obtained with that of  $\text{Si}_{\text{NWs}}\text{-Cu}_{\text{NPs}}$ , followed by  $\text{Si}_{\text{NWs}}$ , and  $\text{Si}_{\text{NWs}}\text{-Co}_{\text{NPs}}$  as the lowest.

### 3.5. Photocatalysis with Rh6G

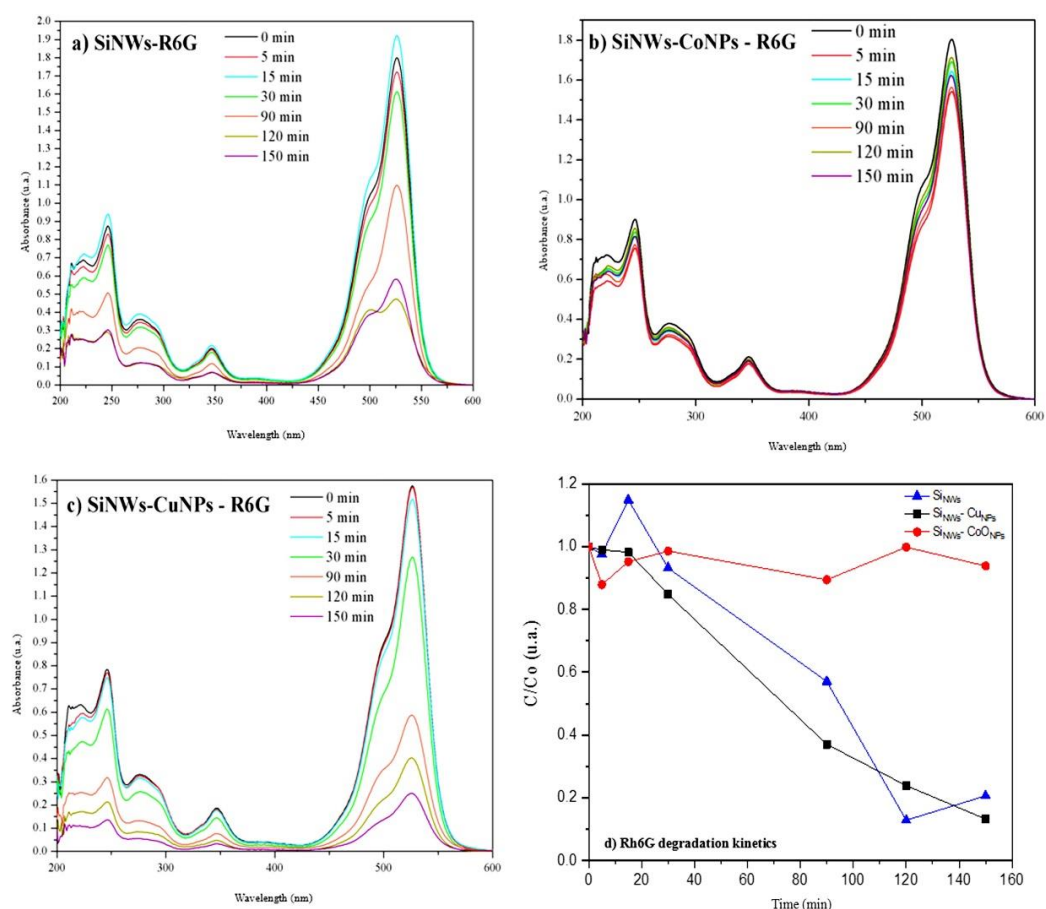
Figure 12 shows the photocatalytic activity in the Rh6G with the  $\text{Si}_{\text{NWs}}$ ,  $\text{Si}_{\text{NWs}}\text{-Co}_{\text{NPs}}$ , and  $\text{Si}_{\text{NWs}}\text{-Cu}_{\text{NPs}}$  with LED light. The Rh6G has its characteristic absorption peak at 526 nm, so as the intensity at that peak decreases with increasing photocatalysis time, dye chemisorption occurs as in the  $\text{Si}_{\text{NWs}}\text{-Cu}_{\text{NPs}}$  spectrum. However, in the  $\text{Si}_{\text{NWs}}$  and  $\text{Si}_{\text{NWs}}\text{-Co}_{\text{NPs}}$  spectra, this peak intensity does not decrease over time.

Figure 12d compares the photocatalytic activities of the three photocatalysts. In this way, the  $\text{Si}_{\text{NWs}}\text{-Cu}_{\text{NPs}}$  had a chemisorption efficiency of 86.88% at 150 min, while the highest chemisorption efficiency of the  $\text{Si}_{\text{NWs}}$  was 87% at 120 min. In the case of the  $\text{Si}_{\text{NWs}}\text{-Co}_{\text{NPs}}$  photocatalyst, its maximum chemisorption efficiency was approximately 12% at minute 5.

On the other hand, the UV-Vis absorption spectra of the photocatalysts show that as the peak decreases at 526 nm, there was no creation of new peaks, so it was attributed that the phenomenon present in Rh6G photocatalysis was not degradation, but the adsorption of organic molecules similarly to MB [60]. Again, similarly to MB, the desorption of the molecules was observed, explaining the increases at certain times of the photocatalysis [16]. The degradation of the Rh6G organic molecule was not achieved due to the lack of potential in the photocatalysts linked to the ability to concentrate charges by the resistivity of the semiconductor. The molecular structure of Rh6G has multiple aromatic rings, which need a sufficient amount of energy to break their bonds.

As with MB, the adsorption and desorption of organic dye molecules occurred, with the most efficient photocatalyst being  $\text{Si}_{\text{NWs}}\text{-Cu}_{\text{NPs}}$ . In the case of  $\text{Si}_{\text{NWs}}$  and  $\text{Si}_{\text{NWs}}\text{-Co}_{\text{NPs}}$  exhibiting dye desorption, there was a reduction in chemisorption efficiency, which was very large in  $\text{Si}_{\text{NWs}}\text{-Co}_{\text{NPs}}$  because the deposited Co nanoparticles probably were oxidized and could be as  $\text{Co}(\text{OH})_2/\text{CoO}$  deposited on the surface. It should be noted that the difference in efficiency between  $\text{Si}_{\text{NWs}}$  and  $\text{Si}_{\text{NWs}}\text{-Co}_{\text{NPs}}$  was minimal.

The reason for the desorption of the dye molecules was attributed to the fact that, in the cathodic regions present on the surface of the nanowires, where there was a considerable accumulation of electrons (negative charge), molecular adsorption was carried out preferably until saturation. However, when these regions lose their charge (electric discharge), the process of desorption occurs because the charge of the molecule was no longer related to the charge on the surface of the nanowires.



**Figure 12.** UV-Vis spectra of Rh6G treatment with the photocatalysts (a) SiNWs, (b) SiNWs-CoONPs, and (c) SiNWs-CuNPs. (d) Rh6G degradation kinetics using SiNWs, SiNWs-CoONPs, and SiNWs-CuNPs as photocatalysts.

### 3.6. Review and Comparison of Photodegradations of MO, MB, and Rh B Dyes by SiNWs

Table 2 shows a brief review of the literature that use SiNWs as photocatalysts with different crystalline orientation, heterojunction with other semiconductors, light sources, target dye molecule, dye concentration in aqueous solutions, treatment time, and degradation efficiencies.

The three dyes (MO, MB, and Rh 6G) have been used as target molecules to evaluate many different photocatalysts. In the case of SiNWs, this table resumes some process parameters but many more cause differences in the degradation efficiencies. Moreover, there is a growing tendency to use heterojunctions with other semiconductors in addition to the variations of metallic decorating nanoparticles. In some cases, there is missing information about these or other parameters, such as the power of illumination, the heating of the aqueous solution, the atmospheric pressure, pulsed illumination, potential in case of photoelectrocatalysis, volume of the samples, area of lighting, and so forth.

The MO degradation kinetics were in the sequence SiNWs-CuNPs (88.9%) > SiNWs (85.3%) > SiNWs-CoONPs (49.3%), with the SiNWs-CuNPs having slightly faster kinetics. However, SiNWs-CoONPs have slow degradation kinetics. In the references of Table 2, there are some of them with higher efficiencies than in this work, included in the last rows, especially using CuNPs. The proposal in this work points to CoO as a more stable photocatalyst than CuO<sub>2</sub>. This does not imply that it has higher degradation efficiencies, which are lower in the conditions tested here. One of the reasons for such results was a lower obtained deposited amount of CoO. According with the EDS quantifications, SiNWs (Ag 3.98%), SiNWs-CuNPs (Ag 2.43%, Cu 3.94%), SiNWs-CoONPs (Ag 2.01%, Co 0.01%), normalizing relative to the silicon content. The deposited nanoparticles, including Cu and

Co, were by electroless without adding an activator, which means that the nanowires own potentials and electron supply regulates, in part, the kinetics and amount of depositions.

**Table 2.** List of reported degradation efficiencies of MO, MB, and Rh B dyes using Si<sub>NWs</sub>.

Silicon Type and Orientation	Photocatalyst Composite	Light Source	Target Molecule	Concentration (mg/L)	Degradation Efficiency (%)	Ref.
p	Cu- Si <sub>NWs</sub>	Visible light LEDs	MO	20.0	92 (150 min)	[12]
p (100)	Pd- Si <sub>NWs</sub>	Visible light	MO	25.0	84.5 (36 h in a fuel cell)	[63]
n (100)	H-Si <sub>NWs</sub>	UV	MO	0.327	93 (200 min)	[18]
p (111)	H-Si <sub>NWs</sub>	UV	MB	0.32	49.35 (200 min)	[18]
p (100)	Si <sub>NWs</sub> /GO	UV	MB	6.4	93 (280 min)	[64]
p (100)	Ag-Si <sub>NWs</sub>	Visible	MB	3.199	~98 (200 min)	[65]
	Si <sub>NWs</sub>	580 nm	MB	31.985	18.4 (120 min)	[53]
	Cu <sub>2</sub> O-Si <sub>NWs</sub>	580 nm	MB	15.99	53.8 (120 min)	[53]
p (100)	Cu-Si <sub>NWs</sub> /NaBH <sub>4</sub>	None	MB	15.99	~96 (10 min)	[66]
	Si <sub>NWs</sub> /GO + H <sub>2</sub> O <sub>2</sub>			6.4	96 (120 min)	[64]
	Si <sub>NWs</sub> /GO			6.4	93 (280 min)	[64]
p (100)	CuO <sub>2</sub> -Si <sub>NWs</sub>	580 nm	MB	0.2 × 10 <sup>-3</sup> M (5 mL)	(100 min)	[67]
p & n (100), (111), (110); 0.7 × 1.5 cm <sup>2</sup> ; 0.02, 5–10, 100 Ω cm	H-Si <sub>NWs</sub>	>420 nm	MB MO	10 <sup>-6</sup> M (4 mL)	(200 min)	[18]
p (100), 1–10 Ω cm	Si <sub>NWs</sub> —AuNPs	>420 nm	Rh B	0.5 × 10 <sup>-6</sup> M (3 mL)	(240 min)	[17]
p (100), 1.2 × 0.8 cm <sup>2</sup> , 0.009–0.01 Ω cm	Si <sub>NWs</sub> —AgNPs Si <sub>NWs</sub> —CuNPs	>420 nm	Rh B	0.5 × 10 <sup>-5</sup> M (2 mL)	(120 min)	[52]
p (100), 2 × 2 cm <sup>2</sup> , 5–10 Ω cm	Si <sub>NWs</sub>	400 nm	Rh B	10	(90 min)	[62]
p (100), 2 × 2 cm <sup>2</sup>	Si <sub>NWs</sub>	>420 nm	Rh B	1 (50 mL)	(300 min)	[68]
p (111)	Si <sub>NWs</sub>	Visible light LEDs	MO, MB, Rh6G	20.0	85.3 (150 min), 86 (90 min), 87 (120 min)	This work
	Cu-Si <sub>NWs</sub>				88.9%, 87.2%, 86.88 (150 min)	
	CoO-Si <sub>NWs</sub>				49.3 (150 min), 17.3 (90 min), 12 (5 min)	

In the case of working with oxides, CuO<sub>2</sub> and CoO, they should not require further processing to maintain stability on multiple runs. Nonetheless, all the known reports show decrements in consecutive tests even considering that the solutions have neither other pollutants nor salts. This is another main reason, together with electron–hole recombinations, for photocatalysis has not been used broadly. One explanation for this is that this process is based on redox reactions, which generate ionic compounds as byproducts. Such charged species increase the double layer around the active sites having cathodic or anodic potentials, which blocks them, in part, causing diminish in efficiencies.

#### 4. Conclusions

The Si<sub>NWs</sub> were synthesized using the MACE method. The Si<sub>NWs</sub>-CuNPs were synthesized by depositing the Cu nanoparticles auto-catalytically. Similarly, the Si<sub>NWs</sub>-CoNPs were synthesized firstly as Co and oxidized in the same process. The nanowires had a length of about 23 μm to 30 μm with a vertical structure on the wafer. They were peak-shaped and spaced.

Silicon wafers have no photocatalytic effect lacking the potential for splitting water or causing redox reactions. Si<sub>NWs</sub>, without Schottky barriers or further doping, have a higher area but keep the silicon characteristics. Si<sub>NWs</sub>, Si<sub>NWs</sub>-CoNPs, and Si<sub>NWs</sub>-CuNPs, prepared

in the described procedure and having Ag at the bottom, manifest the effects shown in this and other works. There were dendritic conformations of the silver nanoparticles at the bottom, originally used for generating the nanowire bundles. This structure type can contribute to faster electron transfer.

In the optical images, there is the phenomenon of interference, observed as iridescent colors, because of the size of the filaments resulting from the MACE method and the space between them, which, as far as we know, this work is the first or between the few that show interference of visible light in the nanostructured bundles. Moreover, there was interference in the plane (3 1 1) for the X-ray diffractograms caused by the coincidence of the  $\text{Cu}\alpha_1$  (1.5604 Å) under grazing incidence with the silicon plane distance.

The EDS analysis confirmed the presence of Co in the samples (oxidized). In the case of  $\text{Si}_{\text{NWs}}\text{-Cu}_{\text{NPs}}$ , the approximate length of the nanowires was between 44  $\mu\text{m}$  and 48  $\mu\text{m}$ . They showed a vertical structure on the plate, homogeneity, and agglomerations between nanowires. The EDS analysis confirmed the presence of Cu.

The XPS analyses on the  $\text{Si}_{\text{NWs}}\text{-CoO}_{\text{NPs}}$  samples show that the deposited of Co was not in metallic form but as  $\text{CoO}_{\text{NPs}}$  or as  $\text{Co}(\text{OH})_2/\text{CoO}$ . The pH bath conditions allowed obtaining  $\text{CoO}_{\text{NPs}}$  instead of metallic cobalt.

In the case of MO, the degradation kinetics of  $\text{Si}_{\text{NWs}}\text{-Cu}$  and  $\text{Si}_{\text{NWs}}$  were almost parallel, with  $\text{Si}_{\text{NWs}}\text{-Cu}_{\text{NPs}}$  having slightly faster kinetics due to the contribution of Cu in photocatalysis.  $\text{Si}_{\text{NWs}}\text{-CoO}_{\text{NPs}}$  were found to have very slow degradation kinetics. This was attributed to the cobalt oxide that, contrary to Cu nanoparticles, did not contribute to the electron–hole separation.

MB and Rh6G showed no degradation of the dye molecules during the tests; instead, there was adsorption and desorption of them. The most efficient photocatalyst was  $\text{Si}_{\text{NWs}}\text{-Cu}_{\text{NPs}}$ . Nonetheless, it should be noted that  $\text{Si}_{\text{NWs}}$  and  $\text{Si}_{\text{NWs}}\text{-Cu}_{\text{NPs}}$  show similar efficiencies.  $\text{Si}_{\text{NWs}}\text{-CoO}_{\text{NPs}}$  show substantially less efficiency.

The photocatalytic activity of this work's materials, the  $\text{Si}_{\text{NWs}}$ ,  $\text{Si}_{\text{NWs}}\text{-Cu}_{\text{NPs}}$ , and  $\text{Si}_{\text{NWs}}\text{-CoO}_{\text{NPs}}$ , depend not only on the materials themselves but also on multiple factors, which alter the kinetics and final efficiencies. Under the conditions reported, with the characteristics described, all the materials were photocatalytic, but in the sequence  $\text{Si}_{\text{NWs}}\text{-Cu}_{\text{NPs}} > \text{Si}_{\text{NWs}} > \text{Si}_{\text{NWs}}\text{-CoO}_{\text{NPs}}$ . Even more, their capability of degrading methyl orange was not replicated for methylene blue and rhodamine 6G, which shows that, in addition to the factors to that sequence, there are others to address when changing the target for decomposing. The tests can be repeated several times, but there is a decrement caused by sorption on the surfaces of ionic byproducts of the decomposition, changes in the oxidation state of  $\text{Cu}_{\text{NPs}}$ , chemical reactions, and various other processes.

**Author Contributions:** Conceptualization, J.d.J.P.B.; methodology O.A.C.C., J.d.J.P.B., Y.C.M., C.H.R., A.X.M.P. and M.R.G.R.; validation, O.A.C.C., J.d.J.P.B. and D.C.A.; formal analysis, O.A.C.C. and J.d.J.P.B.; investigation, O.A.C.C., J.d.J.P.B. and M.R.G.R.; resources, O.A.C.C., J.d.J.P.B., Y.C.M., C.H.R., C.M.L., M.R.G.R., J.G.F.L. and H.R.S.; data curation, O.A.C.C., J.d.J.P.B., C.M.L., J.G.F.L. and H.R.S.; writing—original draft preparation, O.A.C.C., J.d.J.P.B. and D.C.A.; writing—review and editing, J.d.J.P.B., C.H.R., A.X.M.P., M.L.M.L. and G.O.; visualization, O.A.C.C., J.d.J.P.B. and A.X.M.P.; supervision, J.d.J.P.B. and D.C.A.; project administration, J.d.J.P.B. and M.L.M.L.; funding acquisition, J.d.J.P.B. and M.L.M.L. All authors have read and agreed to the published version of the manuscript.

**Funding:** This research was funded by “Fondo Sectorial CONACYT-SENER Sustentabilidad Energética” through Grant 207450, “Centro Mexicano de Innovación en Energía Solar (CeMIESol)”, within strategic project No. P62, “Prototype hybrid system of a supercritical  $\text{CO}_2$  expander with flat polycarbonate mirrors on automated heliostats”. This work was supported by the National Council of Science and Technology CONACYT (México), through the Basic and/or Frontier Science grant No. 320114, the National Laboratory of Graphenic Materials, and the LANIAUTO.

**Informed Consent Statement:** Not applicable.

**Acknowledgments:** The authors thank the CIDETEQ's staff members who supported the processes necessary to carry out the projects and laboratory activities.

**Conflicts of Interest:** The authors declare no conflict of interest.

## References

1. Abebe, B.; Ananda Murthy, H.C.; Dessie, Y. Synthesis and Characterization of Ti-Fe Oxide Nanomaterials: Adsorption-Degradation of Methyl Orange Dye. *Arab. J. Sci. Eng.* **2020**, *45*, 4609–4620. [[CrossRef](#)]
2. Shen, Y.; Zhang, Z.; Xiao, K. Evaluation of Cobalt Oxide, Copper Oxide and Their Solid Solutions as Heterogeneous Catalysts for Fenton-Degradation of Dye Pollutants. *RSC Adv.* **2015**, *5*, 91846–91854. [[CrossRef](#)]
3. Salierno, G.; Napoleone, S.; Maisterrena, A.; Cassanello, M.; Pellasio, M.; Doumic, L.; Ayude, M.A. Continuous Heterogeneous Fenton-Type Process for Dye Pollution Abatement Intensified by Hydrodynamic Cavitation. *Ind. Eng. Chem. Res.* **2021**, *60*, 16653–16664. [[CrossRef](#)]
4. Rizzo, L.; Malato, S.; Antakyali, D.; Beretsou, V.G.; Đolić, M.B.; Gernjak, W.; Heath, E.; Ivancev-Tumbas, I.; Karaolia, P.; Lado Ribeiro, A.R.; et al. Consolidated vs New Advanced Treatment Methods for the Removal of Contaminants of Emerging Concern from Urban Wastewater. *Sci. Total Environ.* **2019**, *655*, 986–1008. [[CrossRef](#)]
5. Johnston, A.L.; Lester, E.; Williams, O.; Gomes, R.L. Understanding Layered Double Hydroxide Properties as Sorbent Materials for Removing Organic Pollutants from Environmental Waters. *J. Environ. Chem. Eng.* **2021**, *9*, 105197. [[CrossRef](#)]
6. Li, C.; Li, J.; Wang, N.; Zhao, Q.; Wang, P. Status of the Treatment of Produced Water Containing Polymer in Oilfields: A Review. *J. Environ. Chem. Eng.* **2021**, *9*, 105303. [[CrossRef](#)]
7. Hernández-Morales, V.; Nava, R.; Acosta-Silva, Y.J.; Macías-Sánchez, S.A.; Pérez-Bueno, J.J.; Pawelec, B. Adsorption of Lead (II) on SBA-15 Mesoporous Molecular Sieve Functionalized with –NH<sub>2</sub> Groups. *Microporous Mesoporous Mater.* **2012**, *160*, 133–142. [[CrossRef](#)]
8. Martínez, M.G.A.; de Jesus Pérez-Bueno, J.; Reza, E.M.; López, M.L.M. Lead Adsorption in Manganese Oxides as Powders and Coatings Supported on Silica Gel Beads and Tin Inverse Opal-Like Structures. *Curr. Anal. Chem.* **2020**, *17*, 831–838. [[CrossRef](#)]
9. Faucher, S.; Aluru, N.; Bazant, M.Z.; Blankschtein, D.; Brozena, A.H.; Cumings, J.; Pedro De Souza, J.; Elimelech, M.; Epsztein, R.; Fourkas, J.T.; et al. Critical Knowledge Gaps in Mass Transport through Single-Digit Nanopores: A Review and Perspective. *J. Phys. Chem. C* **2019**, *123*, 21309–21326. [[CrossRef](#)]
10. Márquez, E.E.; Zarazúa, G.M.S.; Bueno, J.D.J.P. Prospects for the Use of Electrooxidation and Electrocoagulation Techniques for Membrane Filtration of Irrigation Water. *Environ. Process.* **2020**, *7*, 391–420. [[CrossRef](#)]
11. Olea, M.A.U.; Bueno, J.D.J.P.; Pérez, A.X.M. Nanometric and Surface Properties of Semiconductors Correlated to Photocatalysis and Photoelectrocatalysis Applied to Organic Pollutants—A Review. *J. Environ. Chem. Eng.* **2021**, *9*, 106480. [[CrossRef](#)]
12. Robles, M.R.G.; Bueno, J.D.J.P.; Syllas, C.S.A.; López, M.L.M.; Guerrero, F.M. Silver/Silicon Nanowires/Copper Nanoparticles Heterojunction for Methyl Orange Degradation by Heterogeneous Photocatalysis under Visible Irradiation. *MRS Adv.* **2018**, *3*, 3933–3938. [[CrossRef](#)]
13. Magallón-Cacho, L.; Pérez-Bueno, J.J.; Meas-Vong, Y.; Stremsoerfer, G.; Espinoza-Beltrán, F.J. Surface Modification of Acrylonitrile-Butadiene-Styrene (ABS) with Heterogeneous Photocatalysis (TiO<sub>2</sub>) for the Substitution of the Etching Stage in the Electroless Process. *Surf. Coat. Technol.* **2011**, *206*, 1410–1415. [[CrossRef](#)]
14. Garcia, E.M.; Santos, J.S.; Pereira, E.C.; Freitas, M.B.J.G. Electrodeposition of Cobalt from Spent Li-Ion Battery Cathodes by the Electrochemistry Quartz Crystal Microbalance Technique. *J. Power Sources* **2008**, *185*, 549–553. [[CrossRef](#)]
15. Zeferino, R.S.; Pal, U.; De Anda Reues, M.E.; Rosas, E.R. Indium Doping Induced Defect Structure Evolution and Photocatalytic Activity of Hydrothermally Grown Small SnO<sub>2</sub> Nanoparticles. *Adv. Nano Res.* **2019**, *7*, 13–24. [[CrossRef](#)]
16. De Lourdes Ruiz Peralta, M.; Sánchez-Cantú, M.; Puente-López, E.; Rubio-Rosas, E.; Tzompantzi, F. Evaluation of Calcium Oxide in Rhodamine 6G Photodegradation. *Catal. Today* **2018**, *305*, 75–81. [[CrossRef](#)]
17. Amdouni, S.; Cherifi, Y.; Coffinier, Y.; Addad, A.; Zaïbi, M.A.; Oueslati, M.; Boukherroub, R.; Zaïbi, M.A.; Oueslati, M.; Boukherroub, R. Gold Nanoparticles Coated Silicon Nanowires for Efficient Catalytic and Photocatalytic Applications. *Mater. Sci. Semicond. Process.* **2018**, *75*, 206–213. [[CrossRef](#)]
18. Brahiti, N.; Hadjersi, T.; Amirouche, S.; Menari, H.; ElKechai, O. Photocatalytic Degradation of Cationic and Anionic Dyes in Water Using Hydrogen-Terminated Silicon Nanowires as Catalyst. *Int. J. Hydrog. Energy* **2018**, *43*, 11411–11421. [[CrossRef](#)]
19. Hamdi, A.; Boussekey, L.; Roussel, P.; Addad, A.; Ezzaouia, H.; Boukherroub, R.; Coffinier, Y. Hydrothermal Preparation of MoS<sub>2</sub>/TiO<sub>2</sub>/Si Nanowires Composite with Enhanced Photocatalytic Performance under Visible Light. *Mater. Des.* **2016**, *109*, 634–643. [[CrossRef](#)]
20. Ifires, M.; Hadjersi, T.; Chegroune, R.; Lamrani, S.; Moulai, F.; Mebarki, M.; Manseri, A. One-Step Electrodeposition of Superhydrophobic NiO-Co(OH)<sub>2</sub> Urchin-like Structures on Si Nanowires as Photocatalyst for RhB Degradation under Visible Light. *J. Alloys Compd.* **2019**, *774*, 908–917. [[CrossRef](#)]
21. Busra, U.; Omer, C. Free Vibration Analysis Silicon Nanowires Surrounded by Elastic Matrix by Nonlocal Finite Element Method. *Adv. Nano Res.* **2019**, *7*, 99–108. [[CrossRef](#)]
22. Arciga-Duran, E.; Meas, Y.; Pérez-Bueno, J.J.; Ballesteros, J.C.; Trejo, G. Electrochemical Synthesis of Co<sub>3</sub>O<sub>4-x</sub> Films for Their Application as Oxygen Evolution Reaction Electrocatalysts: Role of Oxygen Vacancies. *J. Electrochem. Soc.* **2018**, *165*, H3178–H3186. [[CrossRef](#)]
23. Lu, K.-Q.Q.; Lin, X.; Tang, Z.-R.R.; Xu, Y.-J.J. Silicon Nanowires@Co<sub>3</sub>O<sub>4</sub> Arrays Film with Z-scheme Band Alignment for Hydrogen Evolution. *Catal. Today* **2019**, *335*, 294–299. [[CrossRef](#)]

24. Yang, R.Q.; Ji, Y.C.; Li, Q.; Zhao, Z.H.; Zhang, R.T.; Liang, L.L.; Liu, F.; Chen, Y.K.; Han, S.W.; Yu, X.; et al. Ultrafine Si Nanowires/Sn<sub>3</sub>O<sub>4</sub> Nanosheets 3D Hierarchical Heterostructured Array as a Photoanode with High-Efficient Photoelectrocatalytic Performance. *Appl. Catal. B Environ.* **2019**, *256*, 117798. [[CrossRef](#)]
25. Ghosh, P.; Kar, A.; Khandelwal, S.; Vyas, D.; Mir, A.Q.; Chakraborty, A.L.; Hegde, R.S.; Sharma, S.; Dutta, A.; Khatua, S. Plasmonic CoO-Decorated Au Nanorods for Photoelectrocatalytic Water Oxidation. *ACS Appl. Nano Mater.* **2019**, *2*, 5795–5803. [[CrossRef](#)]
26. Briño-Enriquez, K.M.; Ledesma-García, J.; Perez-Bueno, J.J.; Godínez, L.A.; Terrones, H.; Ángeles-Chavez, C. Bonding Titanium on Multi-Walled Carbon Nanotubes for Hydrogen Storage: An Electrochemical Approach. *Mater. Chem. Phys.* **2009**, *115*, 521–525. [[CrossRef](#)]
27. Ildefonso, Z.T.; José de Jesús, P.B.; Celeste Yunueth, T.L.; Luis, L.R.; Maria Luisa, M.L.; Yunny, M.V. A Phenomenon of Degradation of Methyl Orange Observed during the Reaction of NH<sub>4</sub>TiOF<sub>3</sub> Nanotubes with the Aqueous Medium to Produce TiO<sub>2</sub> Anatase Nanoparticles. *RSC Adv.* **2016**, *6*, 76167–76173. [[CrossRef](#)]
28. Torres, I.Z.; Bueno, J.D.J.P.; López, C.Y.T.; Rojas, L.L.; López, M.L.M.; Vong, Y.M. Nanotubes with Anatase Nanoparticulate Walls Obtained from NH<sub>4</sub>TiOF<sub>3</sub> Nanotubes Prepared by Anodizing Ti. *RSC Adv.* **2016**, *6*, 41637–41643. [[CrossRef](#)]
29. Chen, Y.J.; Zhu, P.F.; Duan, M.; Li, J.; Ren, Z.H.; Wang, P.P. Fabrication of a Magnetically Separable and Dual Z-Scheme PANI/Ag<sub>3</sub>PO<sub>4</sub>/NiFe<sub>2</sub>O<sub>4</sub> Composite with Enhanced Visible-Light Photocatalytic Activity for Organic Pollutant Elimination. *Appl. Surf. Sci.* **2019**, *486*, 198–211. [[CrossRef](#)]
30. Zhu, Y.; Zhang, T.; An, T.; Zong, Y.; Lee, J.Y. Unraveling the Electrocatalytically Active Sites and Stability of Co & Co Oxides on Nanocarbon for Oxygen Evolution Reaction in Acid Solution. *J. Energy Chem.* **2020**, *49*, 8–13. [[CrossRef](#)]
31. Sun, T.; Liu, P.; Zhang, Y.; Chen, Z.; Zhang, C.; Guo, X.; Ma, C.; Gao, Y.; Zhang, S. Boosting the Electrochemical Water Splitting on Co<sub>3</sub>O<sub>4</sub> through Surface Decoration of Epitaxial S-Doped CoO Layers. *Chem. Eng. J.* **2020**, *390*, 124591. [[CrossRef](#)]
32. Shi, W.; Guo, F.; Li, M.; Shi, Y.; Shi, M.; Yan, C. Constructing 3D Sub-Micrometer CoO Octahedrons Packed with Layered MoS<sub>2</sub> Shell for Boosting Photocatalytic Overall Water Splitting Activity. *Appl. Surf. Sci.* **2019**, *473*, 928–933. [[CrossRef](#)]
33. Zhu, S.; Liao, W.; Zhang, M.; Liang, S. Design of Spatially Separated Au and CoO Dual Cocatalysts on Hollow TiO<sub>2</sub> for Enhanced Photocatalytic Activity towards the Reduction of CO<sub>2</sub> to CH<sub>4</sub>. *Chem. Eng. J.* **2019**, *361*, 461–469. [[CrossRef](#)]
34. Boughelout, A.; Macaluso, R.; Kechouane, M.; Trari, M. Photocatalysis of Rhodamine B and Methyl Orange Degradation under Solar Light on ZnO and Cu<sub>2</sub>O Thin Films. *React. Kinet. Mech. Catal.* **2020**, *129*, 1115–1130. [[CrossRef](#)]
35. Rasheed, P.; Haq, S.; Waseem, M.; Rehman, S.U.; Rehman, W.; Bibi, N.; Shah, S.A.A. Green Synthesis of Vanadium Oxide-Zirconium Oxide Nanocomposite for the Degradation of Methyl Orange and Picloram. *Mater. Res. Express* **2020**, *7*, 025011. [[CrossRef](#)]
36. Han, Y.-Q.; Lei, L.; Yang, C.; Zhang, S.-Y.; Zhao, Q.; Zhang, X.-J. Mechanism underlying photocatalyzed degradation of methyl orange by layered black phosphorus. *J. Appl. Ecol.* **2020**, *31*, 333–339. [[CrossRef](#)]
37. Khatri, A.; Rana, P.S. Visible Light Assisted Photocatalysis of Methylene Blue and Rose Bengal Dyes by Iron Doped NiO Nanoparticles Prepared via Chemical Co-Precipitation. *Phys. B Condens. Matter* **2020**, *579*, 411905. [[CrossRef](#)]
38. Sa-Nguanprang, S.; Phuruangrat, A.; Thongtem, T.; Thongtem, S. Preparation of Visible-Light-Driven Al-Doped ZnO Nanoparticles Used for Photodegradation of Methylene Blue. *J. Electron. Mater.* **2020**, *49*, 1841–1848. [[CrossRef](#)]
39. Varnagiris, S.; Urbonavicius, M.; Sakalauskaite, S.; Daugelavicius, R.; Pranevicius, L.; Lelis, M.; Milcius, D. Floating TiO<sub>2</sub> Photocatalyst for Efficient Inactivation of *E. Coli* and Decomposition of Methylene Blue Solution. *Sci. Total Environ.* **2020**, *720*, 137600. [[CrossRef](#)]
40. Haimerl, J.M.; Ghosh, I.; König, B.; Lupton, J.M.; Vogelsang, J. Chemical Photocatalysis with Rhodamine 6G: Investigation of Photoreduction by Simultaneous Fluorescence Correlation Spectroscopy and Fluorescence Lifetime Measurements. *J. Phys. Chem. B* **2018**, *122*, 10728–10735. [[CrossRef](#)]
41. Tang, C.; Chen, C.; Zhang, H.; Zhang, J.; Li, Z. Enhancement of Degradation for Nitrogen Doped Zinc Oxide to Degrade Methylene Blue. *Phys. B Condens. Matter* **2020**, *583*, 412029. [[CrossRef](#)]
42. Van de Linde, S.; Sauer, M. How to Switch a Fluorophore: From Undesired Blinking to Controlled Photoswitching. *Chem. Soc. Rev.* **2014**, *43*, 1076–1087. [[CrossRef](#)] [[PubMed](#)]
43. Pérez-Bueno, J.J.; Vasquez-García, S.R.; García-González, L.; Vorobiev, Y.V.; Luna-Bárceñas, G.; González-Hernández, J. Optical Processes in PMMA, SiO<sub>2</sub>, and Hybrid Organic-Inorganic Sol-Gel Films Colored with Rhodamine 6GDN. *J. Phys. Chem. B* **2002**, *106*, 1550–1556. [[CrossRef](#)]
44. Mirzaei, A.; Kang, S.Y.; Choi, S.W.; Kwon, Y.J.; Choi, M.S.; Bang, J.H.; Kim, S.S.; Kim, H.W. Fabrication and Gas Sensing Properties of Vertically Aligned Si Nanowires. *Appl. Surf. Sci.* **2018**, *427*, 215–226. [[CrossRef](#)]
45. Martínez-Hernández, A.; Méndez-Albores, A.; Arciga-Duran, E.; Flores, J.G.; Pérez-Bueno, J.J.; Meas, Y.; Trejo, G. Effect of Heat Treatment on the Hardness and Wear Resistance of Electrodeposited Co-B Alloy Coatings. *J. Mater. Res. Technol.* **2019**, *8*, 960–968. [[CrossRef](#)]
46. Huang, Z.; Geyer, N.; Werner, P.; De Boor, J.; Gösele, U. Metal-Assisted Chemical Etching of Silicon: A Review. *Adv. Mater* **2011**, *23*, 285–308. [[CrossRef](#)]
47. Franz, M.; Junghans, R.; Schmitt, P.; Szeghalmi, A.; Schulz, S.E. Wafer-Level Integration of Self-Aligned High Aspect Ratio Silicon 3D Structures Using the MACE Method with Au, Pd, Pt, Cu, and Ir. *Beilstein J. Nanotechnol.* **2020**, *11*, 1439–1449. [[CrossRef](#)]
48. Le Nguyen, N.; Phan, T.C.H.; Dang, T.M.D.; Dang, M.C. Formation of Silver Nanoparticles and Their Application for Suppressing Surface Reflection of N-Type Silicon. *Adv. Nat. Sci. Nanosci. Nanotechnol.* **2019**, *10*, 025014. [[CrossRef](#)]

49. Leonardi, A.; Faro, M.; Irrera, A. Silicon Nanowires Synthesis by Metal-Assisted Chemical Etching: A Review. *Nanomaterials* **2021**, *11*, 383. [[CrossRef](#)]
50. Canevali, C.; Alia, M.; Fanciulli, M.; Longo, M.; Ruffo, R.; Mari, C.M. Influence of Doping Elements on the Formation Rate of Silicon Nanowires by Silver-Assisted Chemical Etching. *Surf. Coat. Technol.* **2015**, *280*, 37–42. [[CrossRef](#)]
51. Peng, K.Q.; Hu, J.J.; Yan, Y.J.; Wu, Y.; Fang, H.; Xu, Y.; Lee, S.T.; Zhu, J. Fabrication of Single-Crystalline Silicon Nanowires by Scratching a Silicon Surface with Catalytic Metal Particles. *Adv. Funct. Mater.* **2006**, *16*, 387–394. [[CrossRef](#)]
52. Megouda, N.; Hadjersi, T.; Coffinier, Y.; Szunerits, S.; Boukherroub, R. Investigation of Morphology, Reflectance and Photocatalytic Activity of Nanostructured Silicon Surfaces. *Microelectron. Eng.* **2016**, *159*, 94–101. [[CrossRef](#)]
53. Hsiao, P.H.; Li, T.C.; Chen, C.Y. ZnO/Cu<sub>2</sub>O/Si Nanowire Arrays as Ternary Heterostructure-Based Photocatalysts with Enhanced Photodegradation Performances. *Nanoscale Res. Lett.* **2019**, *14*, 244. [[CrossRef](#)] [[PubMed](#)]
54. Vázquez-Santoyo, L.D.D.; Pérez-Bueno, J.J.J.; Manzano-Ramírez, A.; Gonzalez-Hernández, J.; Pérez-Robles, J.F.F.; Vorobiev, Y.V.V. Origin of Interference Colors on Austenitic Stainless Steel. *Inorg. Mater.* **2005**, *41*, 955–960. [[CrossRef](#)]
55. Akram, N.; Guo, J.; Ma, W.; Guo, Y.; Hassan, A.; Wang, J. Synergistic Catalysis of Co(OH)<sub>2</sub>/CuO for the Degradation of Organic Pollutant Under Visible Light Irradiation. *Sci. Rep.* **2020**, *10*, 1939. [[CrossRef](#)]
56. Sivakov, V.; Kaniukov, E.Y.; Petrov, A.V.; Korolik, O.V.; Mazanik, A.V.; Bochmann, A.; Teichert, S.; Hidi, I.J.; Schleusener, A.; Cialla, D.; et al. Silver Nanostructures Formation in Porous Si/SiO<sub>2</sub> Matrix. *J. Cryst. Growth* **2014**, *400*, 21–26. [[CrossRef](#)]
57. Chiou, A.-H.; Chien, T.-C.; Su, C.-K.; Lin, J.-F.; Hsu, C.-Y. The Effect of Differently Sized Ag Catalysts on the Fabrication of a Silicon Nanowire Array Using Ag-Assisted Electroless Etching. *Curr. Appl. Phys.* **2013**, *13*, 717–724. [[CrossRef](#)]
58. Fewster, P.F. A New Theory for X-Ray Diffraction. *Acta Crystallogr. Sect. A Found. Adv.* **2014**, *70*, 257–282. [[CrossRef](#)]
59. Fraser, J.T.; Wark, J.S. Comments on a New Theory for X-Ray Diffraction. *Acta Crystallogr. Sect. A Found. Adv.* **2018**, *74*, 447–465. [[CrossRef](#)]
60. Sha, Y.; Mathew, I.; Cui, Q.; Clay, M.; Gao, F.; Zhang, X.J.; Gu, Z. Rapid Degradation of Azo Dye Methyl Orange Using Hollow Cobalt Nanoparticles. *Chemosphere* **2016**, *144*, 1530–1535. [[CrossRef](#)]
61. Brik, A.; Naama, S.; Hadjersi, T.; Benamar, M.E.A.; Bouanik, S.; Manseri, A. Photodegradation of Methylene Blue under UV and Visible Light Irradiation by Er<sub>2</sub>O<sub>3</sub>-Coated Silicon Nanowires as Photocatalyst. *React. Kinet. Mech. Catal.* **2020**, *131*, 525–536. [[CrossRef](#)]
62. Ameen, S.; Park, D.R.; Shin, H.S. Silicon Nanowires Arrays for Visible Light Driven Photocatalytic Degradation of Rose Bengal Dye. *J. Mater. Sci. Mater. Electron.* **2016**, *27*, 10460–10467. [[CrossRef](#)]
63. Han, H.X.; Shi, C.; Yuan, L.; Sheng, G.P. Enhancement of Methyl Orange Degradation and Power Generation in a Photoelectrocatalytic Microbial Fuel Cell. *Appl. Energy* **2017**, *204*, 382–389. [[CrossRef](#)]
64. Gaidi, M.; Daoudi, K.; Columbus, S.; Hajjaji, A.; El Khakani, M.A.; Bessais, B. Enhanced Photocatalytic Activities of Silicon Nanowires/Graphene Oxide Nanocomposite: Effect of Etching Parameters. *J. Environ. Sci.* **2021**, *101*, 123–134. [[CrossRef](#)] [[PubMed](#)]
65. Ghosh, R.; Ghosh, J.; Das, R.; Mawlong, L.P.L.L.; Paul, K.K.; Giri, P.K. Multifunctional Ag Nanoparticle Decorated Si Nanowires for Sensing, Photocatalysis and Light Emission Applications. *J. Colloid Interface Sci.* **2018**, *532*, 464–473. [[CrossRef](#)] [[PubMed](#)]
66. Yang, X.; Zhong, H.; Zhu, Y.; Jiang, H.; Shen, J.; Huang, J.; Li, C. Highly Efficient Reusable Catalyst Based on Silicon Nanowire Arrays Decorated with Copper Nanoparticles. *J. Mater. Chem. A* **2014**, *2*, 9040–9047. [[CrossRef](#)]
67. Tang, C.H.; Hsiao, P.H.; Chen, C.Y. Efficient Photocatalysts Made by Uniform Decoration of Cu<sub>2</sub>O Nanoparticles on Si Nanowire Arrays with Low Visible Reflectivity. *Nanoscale Res. Lett.* **2018**, *13*, 312–315. [[CrossRef](#)]
68. Liu, Y.; Ji, G.; Wang, J.; Liang, X.; Zuo, Z.; Shi, Y. Fabrication and Photocatalytic Properties of Silicon Nanowires by Metal-Assisted Chemical Etching: Effect of H<sub>2</sub>O<sub>2</sub> Concentration. *Nanoscale Res. Lett.* **2012**, *7*, 663. [[CrossRef](#)]